



HAL
open science

The Role of Redox Processes in Determining the Iron Isotope Compositions of Minerals, Melts, and Fluids

Paolo A Sossi, Baptiste Debret

► **To cite this version:**

Paolo A Sossi, Baptiste Debret. The Role of Redox Processes in Determining the Iron Isotope Compositions of Minerals, Melts, and Fluids. *Magma Redox Geochemistry*, 2021, 978-1-119-47325-1. hal-03368395

HAL Id: hal-03368395

<https://hal.science/hal-03368395>

Submitted on 20 Oct 2021

HAL is a multi-disciplinary open access archive for the deposit and dissemination of scientific research documents, whether they are published or not. The documents may come from teaching and research institutions in France or abroad, or from public or private research centers.

L'archive ouverte pluridisciplinaire **HAL**, est destinée au dépôt et à la diffusion de documents scientifiques de niveau recherche, publiés ou non, émanant des établissements d'enseignement et de recherche français ou étrangers, des laboratoires publics ou privés.

1 **The role of redox processes in determining the iron isotope compositions of**
2 **minerals, melts and fluids**

3 Paolo A. Sossi^{1,2} and Baptiste Debret^{1,3}

4 ¹ Institut de Physique du Globe de Paris, Université de Paris, 1 rue Jussieu, 75005, Paris, France

5 ² Institute of Geochemistry and Petrology, ETH Zürich, Sonneggstrasse 5, CH-8092, Zürich,
6 Switzerland

7 ³ Laboratoire G-Time, DGES, Université Libre de Bruxelles, ULB, CP 160/02, 1050 Brussels,
8 Belgium

9 **Abstract**

10 Stable isotope fractionation is a response to the minimisation of free energy associated with differences
11 in vibrational frequencies during substitution of isotopic masses between two phases. Site properties
12 are dictated by the bonding environment of iron, and influence its ‘force constant’, a descriptor for bond
13 strength. Because iron readily transitions between its ferrous (Fe²⁺) and ferric (Fe³⁺) state over the
14 oxygen fugacities (fO_2) of terrestrial magmas, redox processes are presumed to control iron isotope
15 fractionation. In fact, both co-ordination and redox state are key to interpreting iron isotope variations
16 in high-temperature, high-pressure geological systems. Determinations of iron force constants by
17 experimental, theoretical and spectroscopic means in minerals, melts and fluids are reviewed,
18 emphasising the effect of composition in influencing isotopic fractionation. Within this framework, the
19 application of numerical models of partial melting to iron isotope variations in oceanic basalts and
20 subduction-zone (or arc) magmas has shed light on their genesis. The influence of melt composition,
21 mineral mode and fluid exsolution in producing iron isotope fractionation in evolving magmas is
22 explored. Iron isotopic signatures in magmatic rocks are linked to that of their sources, and are
23 influenced by the iron isotopic evolution of subducting slabs and transfer of fluids to the mantle wedge.

24 Introduction

25 The existence of iron in three predominant oxidation states in high temperature processes (Fe^0 , Fe^{2+} ,
26 Fe^{3+}) provides considerable scope for the fractionation of its isotopes. This property, together with the
27 fact that iron is the often most abundant polyvalent element in natural systems, has made its isotopic
28 composition the most well-studied of the non-traditional systems (see Dauphas et al. 2017 for a recent
29 comprehensive review).

30 Owing to the role that iron plays in determining the oxygen fugacity ($f\text{O}_2$) of a geological system,
31 variations in its isotopic composition have often been ascribed to changes in its redox state (*e.g.*,
32 Williams et al. 2004; Dauphas et al. 2009). This approach comes at the expense of consideration of the
33 co-ordination of iron, which can have an equally important role in engendering isotopic fractionation
34 (see Young et al. 2015; Sossi and O'Neill, 2017). Furthermore, the oxygen fugacity of a system may
35 have an indirect effect on the iron isotope composition by modifying the stability of different phases
36 and solid solutions (*e.g.*, the precipitation of pyrite from hydrothermal fluids, Wawryk and Foden 2015;
37 or the composition of spinels in solid solution series, Roskosz et al. 2015). Sossi et al. (2016) and Fujii
38 et al. (2014) emphasised the role of co-ordinating ligand field strength (*e.g.*, $-\text{S}$, $-\text{Cl}$, and $-\text{OH}$) in
39 affecting iron isotopic fractionation in minerals and fluids, respectively, by way of changing bond
40 covalence and hence bond stiffness (Hill et al. 2010). Although this effect is limited in terrestrial mafic
41 magmas in which iron is almost exclusively co-ordinated by oxygen, it becomes an important
42 consideration in intermediate- and silicic magmas that can exsolve hydrothermal fluids (see Heimann
43 et al. 2008) and in fluid-loss during mineral breakdown and subsequent dehydration of subducting slabs
44 (see Debret and Sverjensky, 2017).

45 Deconvolving these controls is not straightforward because they tend to be intertwined; for example,
46 simply varying temperature will affect the relative stability of minerals that precipitate from a fluid and
47 these differing assemblages would be reflective of a different $f\text{O}_2$. Similarly, because the Fe^{3+} cation
48 has an ionic radius smaller than that of its ferrous counterpart, it prefers to partition into smaller,
49 tetrahedrally-co-ordinated sites, whereas Fe^{2+} has a greater preference for octahedral sites in melts and
50 minerals (*e.g.*, Wilke 2005). As such, these compounding effects on the magnitude of stable isotope
51 fractionation require careful theoretical (*e.g.*, Schauble et al. 2001), experimental (*e.g.*, Shahar et al.
52 2008) and spectroscopic (*e.g.*, Dauphas et al. 2012) approaches in order to tease out the individual
53 contribution of each.

54 Rather than tackling iron isotopic variation in natural systems by an inverse approach (*i.e.*, through
55 sample measurement and interpretation), in this review, the role of iron oxidation state and co-
56 ordination number in controlling iron isotope fractionation is critically examined from a first-principles
57 perspective (section 2.0.). In order to do so, the methods by which equilibrium iron isotope fractionation
58 factors can be determined, and a compilation of existing data are briefly reviewed (section 3.0.). A

59 general introduction to the ways in which iron isotope fractionation between minerals, melts and fluids
 60 depend on redox processes is presented in section 4.0. Finally, how these determinations have been
 61 applied to interpret variation in natural systems, comprising partial melting, magmatic differentiation
 62 and fluid transfer in the crust and mantle is detailed (section 5.0).

63 2.0. Principles and nomenclature

64 Ratios of two isotopes, n and d of an element, E , are generally expressed relative to their ratio in a
 65 standard in delta notation, which is given by:

$$66 \quad \delta^{n/d}E = \left(\frac{(^{n/d}E)_{\text{sample}}}{(^{n/d}E)_{\text{standard}}} - 1 \right) \times 1000. \quad (1)$$

67 The fractionation factor between two phases A and B is:

$$68 \quad \Delta^{n/d}E_{A-B} = \delta^{n/d}E_A - \delta^{n/d}E_B, \quad (2)$$

69 and is related to alpha notation by the equivalence:

$$70 \quad \Delta^{n/d}E_{A-B} = 10^3 \ln ^{n/d}\alpha_{A-B} \quad (3)$$

71 The exchange of isotopes between two phases, A and B , can be written:



73 The equilibrium distribution of isotopes between the two phases is described by the fractionation factor,
 74 α :

$$75 \quad \alpha^{n/d}E_{A-B} = \frac{(^{n/d}E)_A}{(^{n/d}E)_B}. \quad (5)$$

76 When the B phase consists of solely dissociated atoms of element E (as in an ideal, monatomic gas),
 77 the fractionation factor is given the name beta factor (or β factor) and represents a convenient way of
 78 normalising fractionation factors to a '0' value (as there is no energy associated with isotopic
 79 substitution in a dissociated monatomic element, E^0). For cases in which the stoichiometric coefficients
 80 are unity, equation (5) is equivalent to an equilibrium constant. Therefore, the free energy of the isotopic
 81 substitution at equilibrium can be described:

$$82 \quad \Delta G_{(5)}^0 = -RT \ln \left(\alpha^{n/d}E_{A-B} \right). \quad (6)$$

83 At the conditions (temperature, T ; pressure, P) relevant to magmatic processes, classical
 84 thermodynamic terms cancel and isotopic fractionation is broadly onset by differences in the energy
 85 associated with vibrational frequencies in molecules and in condensed phases among one another. In
 86 the harmonic approximation, these vibrational energies ($E_{vib,i}$) are quantised into n equally-spaced

87 levels, where the finite minimum half quantum of energy that arises from the uncertainty in the positions
 88 and momenta that a particle, i , could occupy in its ground state ($n = 0$), corresponds to the 'zero-point'
 89 energy:

$$90 \quad E_{vib,i} = \left(n_i + \frac{1}{2}\right)h\nu_i. \quad (7)$$

91 Here, h is Planck's constant and ν_i is the vibrational frequency. Because, even at 1000 K, as given by
 92 the Boltzmann equation, particles occupy vanishingly small amounts of their excited states ($n > 0$), the
 93 differences in vibrational frequencies between two isotopes is solely controlled by differences in zero-
 94 point energies. For changes in pressure, the relationship between the mode Gruneisen parameter ($\gamma_{G,i}$),
 95 the vibrational frequency and molar volume (V) at constant temperature in the quasi-harmonic
 96 approximation (Polyakov and Kharlashina 1994), leads to a predictable increase in frequency with
 97 pressure due to contracting molar volumes:

$$98 \quad \left(\frac{\partial \ln \nu_i}{\partial \ln V}\right) = -\gamma_{G,i}. \quad (8)$$

99 As volume changes induced by isotopic substitutions are typically small, correspondingly large pressure
 100 variations are required to significantly influence isotopic fractionation. Frequencies for a simple
 101 diatomic molecule (or, approximately, a mean completely symmetric case) are given by:

$$102 \quad \nu_i = \frac{1}{2\pi} \sqrt{\frac{K}{\mu}} \quad (9)$$

103 Where K is the force constant of vibration and μ the reduced mass. The derivation of the dependence
 104 of isotopic fractionation on the vibrational frequencies of molecules was first expressed by Urey (1947)
 105 and Bigeleisen and Mayer (1947) in the harmonic approximation in terms of the vibrational isotopic
 106 partition function:

$$107 \quad Q_{vib,i} = \prod_i \frac{e^{\left(-\frac{h\nu_i}{2kT}\right)}}{1 - e^{\left(-\frac{h\nu_i}{kT}\right)}}. \quad (10)$$

108 Equation (10) is the product across all vibrational frequencies ν_i for a given isotope in a given phase,
 109 where k is Boltzmann's constant and T absolute temperature. Ratios of vibrational partition functions
 110 may be equated to fractionation factors in a simplified manner (Urey 1947; Bigeleisen and Mayer 1947):

$$111 \quad 10^3 \ln \alpha^{\frac{n}{d}} E_{A-B} = \Delta^{\frac{n}{d}} E_{A-B} = \frac{10^3 3N}{96} \left(\frac{h}{\pi kT}\right)^2 \left(\frac{1}{m_d} - \frac{1}{m_n}\right) [K_A - K_B]. \quad (11)$$

112 Here, K_A and K_B refer to the iron force constants in phases A and B, respectively, m_d and m_n the atomic
 113 masses of the denominator (d) and numerator (n) isotopes, respectively and the $3N$ term (Avogadro's
 114 Number) comes from summation over all vibrations in condensed matter (Bigeleisen and Mayer, 1947).

115 Equation (11) states that the isotopic fractionation at the high temperature limit ($T \rightarrow \infty$) will approach
 116 zero. For a particular element and isotope ratio, most of the equation reduces to a constant term,
 117 yielding, for $^{57/54}\text{Fe}$:

$$118 \quad \Delta^{57}\text{Fe}_{A-B} = 4284 \frac{[K_A - K_B]}{T^2}. \quad (12)$$

119 Equally, for $^{56/54}\text{Fe}$;

$$120 \quad \Delta^{56}\text{Fe}_{A-B} = 2904 \frac{[K_A - K_B]}{T^2}. \quad (13)$$

121 In order to minimise the higher free energy of bonds with higher vibrational frequencies (eq. 9), the
 122 heavier isotope is favoured over the lighter one.

123 In general, higher force constants occur in bonding environments with (see Schauble 2004; Young et
 124 al. 2015; Sossi et al. 2016):

- 125 i) higher oxidation state
- 126 ii) lower co-ordination number
- 127 iii) covalent bonds
- 128 iv) low spin vs. high spin (for Fe and other transition metals)

129 To a first order, the first three controls may be estimated empirically to derive values of K (see Young
 130 et al. 2015; Sossi and O'Neill, 2017), considering that the interactions between cations and anions in a
 131 lattice site can be described quantitatively with ionic interactions. Variations of K then arise due to a
 132 change in the charge and co-ordination of the cation, which are described by the bond valence principle
 133 (Pauling 1929):

$$134 \quad \bar{s} = \frac{\bar{Z}}{C_N}. \quad (14)$$

135 In this equation, \bar{s} is the bond valence, \bar{Z} is the average charge on the cation, and \bar{C}_N the mean co-
 136 ordination number in the mineral. The force constant is then approximated by solving the Born-Landé
 137 equation, after Young et al. (2009), which describes the elastic energy of an ionic lattice:

$$138 \quad K_{f,Fe,O} = - \frac{\bar{s}_{Fe} \bar{s}_O q^2 (1-B)}{4\pi\epsilon_0 r^3}, \quad (15)$$

139 where q is the charge on an electron (1.602×10^{-19} C), B is the Born exponent, dependent on lattice
 140 compressibility (taken to be 12 for minerals), $1/4\pi\epsilon_0$ is Coulomb's constant ($9 \times 10^9 \text{ Nm}^2/\text{C}^2$) and r is
 141 the bond length in metres. More quantitative methods for estimating for K are described in section 3.0.

142 3.0. Methods for the calibration of iron isotope fractionation factors

143 The quantity that drives isotope fractionation, the value of the force constant (*cf.* eq. 15), may be
144 calibrated *via* a variety of methods. These include calculating the structure of the phase (theoretical
145 approaches) or by measuring the force constant (spectroscopic methods). Alternatively, methods that
146 involve measurement of the isotopic composition of two or more phases in equilibrium with one another
147 to determine fractionation factors (experimental approaches) are also widely used. All three are
148 described briefly below.

149 3.1. Theoretical

150 *Ab-initio* simulations are the most common way of determining vibrational frequencies, typically with
151 density functional theory (DFT; *e.g.*, Schauble, 2004), one such class of these computations. DFT
152 models the electronic structure and density of electrons in individual atoms to find the most probable
153 equilibrium ground state electronic configuration. Once this state is defined for a system consisting of
154 x number of atoms, the interatomic distances between them define a molecular structure from which the
155 force constants are calculated. The interested reader is referred to Blanchard and Dauphas (this volume)
156 for a fuller description of the method. A simplified calculation based on the bond valence principle can
157 also yield accurate force constants (eq. 15; Young et al., 2015, 2009; Sossi and O'Neill 2017), though
158 it uses the atomic structure of the phase as an input parameter.

159 3.2. Experimental

160 Here, the phases of interest are synthesised by subjecting a known composition to a specific pressure
161 and temperature. The isotopic composition of one of the resultant phases is measured with respect to
162 that of a second phase, yielding the fractionation factor, $\alpha^d E_{A-B}$. That the two phases grown
163 experimentally are in equilibrium with one another may be determined by two different means: (i)
164 chemical and isotopic equilibrium is demonstrated to have been obtained between the phases of interest
165 (*e.g.*, by time-series and reversal experiments) and (ii) by the three isotope method (Shahar et al. 2008).
166 Here, a series of experiments that approach equilibrium are performed, and the true equilibrium
167 composition is calculated by extrapolation of the experiments to the known bulk composition.
168 Considerations in designing and interpreting the results of experimentally-determined isotopic
169 fractionation are summarised in Shahar et al. (2017) and in Bourdon et al. (2018).

170 3.3. Spectroscopic

171 Measurement of force constants relies upon the excitation of the vibrational modes of motion of the
172 mineral lattice by incoming X-rays which collide with a ^{57}Fe nucleus (the only iron isotope sensitive to
173 this effect). Such information can be determined by Mössbauer spectroscopy (Polyakov and Mineev
174 2000) or by Nuclear-Inelastic Resonant X-Ray Scattering, NRIXS (Polyakov et al. 2007; Dauphas et
175 al. 2012). The latter method is preferred because the characteristics of the impacting photons can be

176 tuned and scanned for purpose at a synchrotron. Both of these methods are dealt with in more detail in
 177 Blanchard and Dauphas (this volume).

178 **4.0. Fundamental controls on isotopic fractionation between minerals, melts and fluids**

179 *4.1. Minerals*

180 The $\text{Fe}^{3+}/\Sigma\text{Fe}$ ratio in minerals is controlled by the stoichiometry of the phase. Some series display
 181 complete solid solution between compositional end-members, and common igneous examples include:

182 i) Magnetite-Ulvöspinel: ${}^{\text{IV}}\text{Fe}^{3+}\text{VI}(\text{Fe}^{2+}\text{Fe}^{3+})\text{O}_4 - {}^{\text{IV}}\text{Fe}^{2+}\text{VI}(\text{Fe}^{2+}\text{Ti}^{4+})\text{O}_4$

183 Magnetite has a complete solid solution with ulvöspinel, an exchange that forms the basis for the Fe-Ti
 184 exchange oxybarometer of Buddington and Lindsley (1964) (see also Arató and Audétat, this volume).
 185 Both are spinel group minerals *sensu lato*, with the general formula AB_2O_4 , where, if the B cations
 186 occupy both the tetrahedral and octahedral sites, the structure is said to be ‘inverse’. Magnetite is a 2-3
 187 spinel (one 2+ cation with two 3+) and has an inverse cation distribution at room temperatures, though
 188 it tends to the random distribution at magmatic temperatures around 1000°C (Wu and Mason 1981).
 189 Ulvöspinel, a 4-2 spinel, also has an inverse structure with Ti exclusively occupying the octahedral site
 190 while ferrous iron is both VI- and IV-fold co-ordinated. Intermediate compositions have site
 191 distributions that are temperature-dependent and are controlled by electron exchange between the two
 192 valence states of Fe, with the random distribution being favoured at higher temperature (O’Neill and
 193 Navrotsky 1984; Wechsler et al. 1984; Bosi et al. 2009).

194 Shahar et al. (2008) determined the fractionation factor between magnetite and fayalite experimentally
 195 in a piston cylinder to be $\Delta^{57}\text{Fe}_{\text{mag-fay}} = +0.30 \times 10^6/\text{T}^2$, reflecting the preference of heavier iron for the
 196 stronger, Fe^{3+} -bearing IV- and VI-fold sites of magnetite relative to the exclusively octahedral ferrous
 197 iron in fayalite. Sossi and O’Neill (2017) measured the fractionation factor between magnetite and
 198 $\text{FeCl}_2 \cdot 4\text{H}_2\text{O}$ fluid in piston cylinder experiments in Ag capsules at 800°C. They estimated the magnetite-
 199 ulvöspinel fractionation factor from fits to their experimental data using bond valence theory, giving
 200 $\Delta^{57}\text{Fe}_{\text{mag-usp}} = +0.32 \times 10^6/\text{T}^2$ (Fig. 1), very similar to that measured between magnetite and fayalite.
 201 There is considerable disagreement as to the force constant of Fe bonds in magnetite; Polyakov et al.
 202 (2007) report a value of 228 N/m calculated from NRIXS spectra, similar to that given thereafter by
 203 Dauphas et al. (2012), 230 N/m, using the same technique. Roskosz et al. (2015) report a higher value
 204 of 264 N/m using NRIXS via extrapolation of trends based on solid solutions of Mg-Fe-Al-Cr spinels,
 205 and they note that discrepancies may be due to the quality of the spectra at high energies and the energy
 206 range over which spectra are collected. Importantly, though the absolute force constants may vary, the
 207 magnitude of mineral-mineral fractionation factors in these studies are in good agreement.

208 ii) Ilmenite-Hematite: ${}^{\text{VI}}\text{Fe}^{2+}\text{TiO}_3 - {}^{\text{VI}}\text{Fe}^{3+}_2\text{O}_3$

209 Iron passes from entirely ferrous to entirely ferric along the solid solution series, whilst remaining in
 210 octahedral co-ordination (*e.g.*, Wechsler and Prewitt 1984). Ilmenite shows limited solid solution with
 211 hematite at the fO_2 s typical of igneous systems, where X_{ilm} varies from 0.98 at 2 log units below the
 212 Fayalite-Magnetite-Quartz (FMQ) buffer to 0.90 at $\Delta FMQ+1$ during crystallisation of a dry tholeiitic
 213 ferrobasalt (see Toplis and Carroll 1995).

214 Determinations of force constants in hematite via Mössbauer spectroscopy (Polyakov and Mineev 2000)
 215 *ab-initio* calculations (Blanchard et al. 2009) and NRIXS (Polyakov et al. 2007; Dauphas et al. 2012)
 216 are all in good agreement, and yield mean Fe-O force constants of between 235 and 252 N/m. Note that
 217 the spinel trend measured in Roskosz et al. (2015) yields higher values for the purely ferric iron-bearing
 218 endmembers, 303 ± 6 N/m ($n = 3$). Polyakov and Mineev (2000) report a force constant for ilmenite of
 219 90 N/m, and hence a fractionation factor of $\Delta^{57/54}Fe_{hem-ilmenite} = 4284(235 - 90)/T^2 = 0.61 \times 10^6/T^2$. Sossi
 220 and O'Neill (2017) measured the isotopic fractionation between ilmenite and $FeCl_2 \cdot 4H_2O$ fluid at 800
 221 °C, and estimated the ilmenite-hematite fractionation factor from fits to their experimental data using
 222 bond valence theory to give $0.58 \times 10^6/T^2$ (Fig. 1). Both fractionation factors are in very good agreement
 223 and highlight the importance of mineral composition within a solid solution in determining the isotopic
 224 fractionation factor.

225 iii) Almandine-Pyrope: $^{VIII}Fe^{2+}_3^{VI}Al_2[SiO_4]_3 - ^{VIII}Mg_3^{VI}Al_2[SiO_4]_3$; Grossular-Andradite:
 226 $^{VIII}Ca_3^{VI}Al^{3+}_2[SiO_4]_3 - ^{VIII}Ca_3^{VI}Fe^{3+}_2[SiO_4]_3$

227 Ferrous iron is dodecahedrally-co-ordinated by oxygen in almandine garnet, a rarity among Fe-bearing
 228 minerals, in which it typically occupies VI-fold sites. Ferric iron in andradite garnet is in octahedral co-
 229 ordination.

230 Sossi and O'Neill (2017) reported fractionation factors between almandine and other Fe-bearing
 231 minerals and showed that its iron isotope composition was invariably lighter than all other phases
 232 investigated (including $FeCl_2$ fluid) by virtue of its longer Fe-O bonds (average of 2.37 Å). They
 233 calculated a force constant of 147 N/m for almandine (Fig. 1). No measurements of force constants or
 234 fractionation factors involving andradite garnet are presently available. However, natural andradite-
 235 bearing garnets show heavier iron isotope compositions relative to their ferrous iron-bearing
 236 counterparts (Urosevic et al. 2018) while garnet is almost always the isotopically lightest phase in
 237 eclogitic rocks (Williams et al. 2009; Huang et al. 2019), reflecting their generally low $Fe^{3+}/\Sigma Fe$ in
 238 mafic and ultramafic rocks (<0.1 ; Williams et al. 2009; Berry et al. 2010).

239 iv) Aegirine-Hedenbergite: $Na^{VI}Fe^{3+}Si_2O_6 - Ca^{VI}Fe^{2+}Si_2O_6$

240 The coupled substitution $NaFe^{3+}(CaFe^{2+})^{-1}$ across the aegirine (acmite)-hedenbergite series involves a
 241 change in ferric to ferrous iron in the same octahedral crystallographic site (the M1 site). This transition

242 is associated with an increase in mean Fe-O bond length from 2.05 Å in aegirine to 2.15 Å in
243 hedenbergite at igneous temperatures of $\approx 1000^\circ\text{C}$ (see Cameron et al. 1973).

244 Both end-members of the series were analysed by Mössbauer spectroscopy and force constants
245 calculated according to the second-order Doppler shift by Polyakov and Mineev (2000), yielding 274
246 N/m for aegirine and 112 N/m for hedenbergite, the latter being similar to other $^{57}\text{Fe}^{2+}$ -bearing silicates
247 determined in the same study (olivine, diopside and enstatite; Polyakov and Mineev 2000). More
248 importantly, the fractionation factor between the two is then $\Delta^{57/54}\text{Fe}_{\text{aeg-hed}} = 0.68 \times 10^6/T^2$, similar in
249 magnitude to that for the exchange of octahedral Fe^{2+} and Fe^{3+} in the ilmenite-hematite series (Fig. 1).

250 v) Riebeckite-Glaucophane: $\text{Na}_2^{\text{VI}}(\text{Mg},\text{Fe}^{2+})_3^{\text{VI}}\text{Fe}^{3+}_2\text{Si}_8\text{O}_{22}(\text{OH})_2$
251 $\text{Na}_2^{\text{VI}}(\text{Mg},\text{Fe}^{2+})_3\text{Al}^{3+}_2\text{Si}_8\text{O}_{22}(\text{OH})_2$

252 Riebeckite-group amphiboles are typically found in alkaline magmatic rocks (*cf.* Schoenberg et al.
253 2009). They can contain between 100% and 40% of their Fe as Fe^{3+} , in which ferric iron is ordered on
254 the M2 site and small amounts on the M1 (Hawthorne 1978) whereas glaucophane hosts ferrous iron
255 exclusively, and is distributed across its M1 and M3 sites.

256 From Mössbauer spectroscopy data, Schoenberg et al. (2009) calculated the beta factors for two
257 riebeckitic amphiboles with $\text{Fe}^{3+}/\Sigma\text{Fe}$ of 0.46 and 0.44, and found $10^3\ln\beta^{57/54}\text{Fe}_{\text{rbk}} = 0.90$ and $0.74 \times$
258 $10^6/T^2$ respectively, which correspond to force constants of 214 and 175 N/m.

259 vi) Spinel group; hercynite – ferrochromite – magnetite $^{\text{IV}}\text{Fe}^{2+}\text{Al}_2\text{O}_4 - ^{\text{IV}}\text{Fe}^{2+}\text{Cr}_2\text{O}_4 - ^{\text{IV}}\text{Fe}^{3+}$
260 $^{\text{VI}}[\text{Fe}^{2+}\text{Fe}^{3+}]\text{O}_4$

261 Spinel-group minerals are ubiquitous in terrestrial mafic and ultramafic lithologies (*e.g.*, Barnes and
262 Roeder 2001) and show extensive solid solutions with first-row transition metals representing the A and
263 B cations (O'Neill and Navrotsky 1984). Natural spinels tend to exhibit Cr-Al or Fe^{3+} -Cr exchange,
264 with a paucity of Fe^{3+} -Al spinels caused by positive deviations from ideality and hence a solvus in the
265 binary system (*e.g.*, Petric et al. 1981; Nell et al. 1989). Chromium, owing to its high octahedral site
266 preference energy $(6/5\Delta_{\text{Oct}})^1$, is strongly ordered onto the octahedral site, conferring a normal cation
267 distribution on the spinel structure, meaning Fe^{2+} is found exclusively on the tetrahedral site. Similarly,
268 Fe^{3+} is displaced from the octahedral site in magnetite to the tetrahedral site with increasing
269 ferrochromite component (O'Neill and Navrotsky 1984).

270 Spinel group minerals are generally found in association with olivine, for example in mantle peridotites and in
271 komatiitic magmas, and are used together with orthopyroxene to determine oxygen fugacities (*e.g.*,
272 Woodland et al. 1992). In reciprocal solid solution with Fe-Mg olivine, Fe^{2+} substitution is favoured

¹ In crystal field theory, Δ_{Oct} relates to the energy difference between the *d*-shell electrons that are split into the e_g and t_{2g} orbitals. For an octahedral field, t_{2g} orbitals are stabilised with respect to the barycentre by $2/5\Delta_{\text{Oct}}$ and e_g by $-3/5\Delta_{\text{Oct}}$. Thus, the minimum Δ_{Oct} is 0 (*e.g.*, Zn^{2+} , Cu^+) and the maximum is $6/5\Delta_{\text{Oct}}$ (*e.g.*, V^{2+} , Cr^{3+}).

273 such that $\text{Cr}/(\text{Cr}+\text{Al})$ increases with increasing $\text{Fe}^{2+}/(\text{Fe}^{2+}+\text{Mg})$ (e.g., Poustovetov and Roeder 2000).
 274 At high Fe^{3+} contents, the spinel structure inverts and extensive exchange with Ti occurs as discussed
 275 above.

276 In a comprehensive study of the effect of solid solution on the mean strength of the Fe-O bonds, Roskosz
 277 et al. (2015) determined the force constants for eight spinel-group minerals. They focused largely on
 278 Mg-Al-Fe spinels with variable $\text{Fe}^{3+}/\sum\text{Fe}$ ratios, from 0 to 1, and one magnesiochromite composition.
 279 Their results show that the Fe-O force constant is linearly correlated with $\text{Fe}^{3+}/\sum\text{Fe}$ with only subsidiary
 280 influence from other structural parameters, ranging from 207 ± 14 in Fe^{2+} -bearing spinels to 303 ± 6
 281 N/m ($n = 3$) for solely ferric iron-bearing spinels (Fig. 2). These values compare with Fe-O force
 282 constants of $197 - 165$ N/m for $^{\text{VI}}\text{Fe}^{2+}$ -bearing silicates (average = 181 ± 15 N/m, $n = 4$), namely olivine
 283 and orthopyroxene (Roskosz et al. 2015), and hence $\Delta^{57/54}\text{Fe}_{\text{sp(FeII)-sil(FeII)}} = 0.11 \pm 0.08 \times 10^6/T^2$. In
 284 attempting to characterise the influence of co-ordination environment on iron isotopic fractionation,
 285 Sossi and O'Neill (2017) determined the fractionation factor between two spinels; hercynite (FeAl_2O_4)
 286 and chromite (FeCr_2O_4) and $\text{FeCl}_2 \cdot 4\text{H}_2\text{O}$ fluid at 800°C . They calculated force constants of 238 N/m
 287 and 225 N/m, respectively, higher than that of fayalite (178 N/m), yielding $\Delta^{57/54}\text{Fe}_{\text{sp(FeII)-sil(FeII)}} = 0.21 \times$
 288 $10^6/T^2$, reflecting the influence of IV-fold vs. VI-fold co-ordination of Fe in spinel and olivine,
 289 respectively (Fig. 1). Compilation of spinel-olivine fractionation factors measured in peridotitic rocks
 290 show generally positive $\Delta^{57/54}\text{Fe}_{\text{sp-ol}}$ at low Cr# (molar $\text{Cr}/(\text{Cr}+\text{Al}+\text{Fe}^{3+})$) compared with negligible or
 291 slightly negative $\Delta^{57/54}\text{Fe}_{\text{sp-ol}}$ at high Cr# (Zhang et al. 2019), in qualitative agreement with lowering of
 292 the force constant in chromite with respect to hercynite (Sossi and O'Neill, 2017) though a change in
 293 sign is not predicted.

294 vii) Bridgmanite – Ferropericlasite $^{\text{VIII}}(\text{Fe}^{2+}, \text{Mg}^{2+}, \text{Fe}^{3+})^{\text{VI}}(\text{Fe}^{3+}, \text{Al}^{3+}, \text{Si}^{4+})\text{O}_3 - ^{\text{VI}}\text{Fe}_x(\text{Mg}_{1-x})\text{O}$

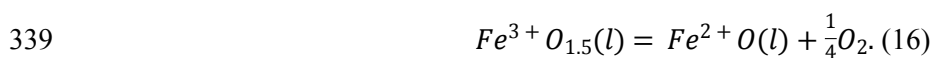
295 Though not a solid solution, it is instructive to assess the body of work for these two minerals given
 296 their importance for controlling iron isotopic fractionation in the Earth's lower mantle. Iron is present
 297 primarily as ferrous iron in the octahedral site of ferropericlasite (cubic) and as Fe^{2+} and Fe^{3+} in the
 298 dodecahedral A and octahedral B sites of bridgmanite (orthorhombic). The substitution of ferric iron
 299 into bridgmanite is strongly facilitated through its coupled substitution with Al^{3+} (McCammon 1997),
 300 which forces Fe^{3+} onto the dodecahedral site by the mechanism $^{\text{VIII}}(\text{Fe}^{2+}, \text{Mg}^{2+})^{\text{VI}}\text{Si}^{4+} \leftrightarrow ^{\text{VIII}}\text{Fe}^{3+}\text{VI}\text{Al}^{3+}$
 301 (Vanpeteghem et al. 2006).

302 Further, the variety of iron spin transitions in lower mantle minerals leads to additional electronic
 303 configurations that modify $\langle\text{Fe-O}\rangle$ bond lengths and therefore influence isotopic fractionation. At low
 304 pressures, the crystal field splitting energy (see footnote 1) is lower than that required to pair electrons,
 305 meaning iron exists in its high spin (HS) configuration. However, compression at lower mantle
 306 pressures reduces the interatomic distance between Fe and O, destabilising the e_g orbitals and making
 307 electron spin pairing energetically more favourable, resulting in a low spin (LS) configuration. This

308 effect is most prevalent in the octahedral sites of ferroperricite and bridgmanite for Fe^{2+} and Fe^{3+}
 309 respectively (see Lin et al. 2013 for a review). Along a mantle adiabat, $^{56}\text{Fe}^{2+}$ in ferroperricite begins
 310 the transition from HS to LS near 60 GPa (Badro et al. 2003; Wentzcovitch et al. 2009) and is complete
 311 by 120 GPa. The transformation is displaced to lower pressures for $^{56}\text{Fe}^{3+}$ in bridgmanite, occurring
 312 over a range from 30 – 70 GPa (Jackson et al. 2005a; Fujino et al. 2012), while $^{56}\text{Fe}^{2+}$ experiences a
 313 spin transition only under very high pressures (> 120 GPa; Badro et al. 2004; McCammon et al. 2010).
 314 Rustad and Yin (2009), using DFT simulations, recorded a systematic increase in force constant for
 315 ferroperricite ($10^3 \ln \beta^{57/54}\text{Fe}_{\text{fp}} = 0.145$ at 4000 K for low spin at 120 GPa and 0.098 for high spin),
 316 corresponding to force constants of ≈ 540 N/m and ≈ 365 N/m, respectively. By contrast, no such shift
 317 was observed for purely Fe^{2+} -bearing bridgmanite due to the asymmetric distortion of the iron-oxygen
 318 bonds, and has $10^3 \ln \beta^{57/54}\text{Fe}_{\text{bg}}$ identical to that of ferroperricite in its LS state. Force constants derived
 319 from Polyakov (2009) for $\text{Fe}_{0.25}\text{Mg}_{0.75}\text{O}$ ($P = 0 - 109$ GPa) and from (Shahar et al. 2016) for FeO ($P =$
 320 $5 - 39$ GPa) using NRIXS yield very similar pressure-dependencies; $K_{\text{Fe-O}} = (2.39 \pm 0.17)P$ (GPa) +
 321 164 ± 10 N/m and $(2.56 \pm 0.16)P$ (GPa) + 169 ± 4 N/m, respectively. If extrapolated linearly to 120 GPa,
 322 these calibrations yield $K_{\text{Fe-O}}$ between 450 and 475 N/m, lower than that calculated by Rustad and Yin
 323 (2009) for LS ferroperricite. Williams et al. (2012) reported the first direct measurement of the iron
 324 isotope composition of experimentally-synthesised Al-bearing (≈ 0.23 per formula unit, pfu)
 325 bridgmanite, with $\text{Fe}^{3+}/\sum\text{Fe} \sim 0.37$ in equilibrium with iron metal at 24 GPa and 1850 °C. Their preferred
 326 $\Delta^{57/54}\text{Fe}_{\text{bg-met}}$ is +1.35 ‰, whose sense is in accord with recent NRIXS determinations of Yang et al.
 327 (2019), though the magnitude is much larger ($\Delta^{57/54}\text{Fe}_{\text{bg-met}}$ by NRIXS is +0.2 ‰ at 2000 K and 30 GPa).
 328 These authors collected an extensive set of *in-situ* high-pressure data for ferroperricite ($\text{Fe}_{0.25}\text{Mg}_{0.75}\text{O}$)
 329 and bridgmanites (both Al-free and Al-bearing at 0.11 pfu). Bridgmanite reaches a maximum $K_{\text{Fe-O}}$ of
 330 449 ± 46 N/m (46 GPa), and is isotopically heavier than ferroperricite below 60 GPa, after which the
 331 latter transitions to its LS state that produces a drastic increase in force constant with a slope of $dK_{\text{Fe-O}}$
 332 $/dP$ of ~ 3 N/m/GPa, reaching 626 ± 31 N/m at 94 GPa. Above 60 GPa, the force constant of
 333 bridgmanite is unchanging around 335 ± 15 N/m up to 104 GPa, independent of $\text{Fe}^{3+}/\sum\text{Fe}$ and Al
 334 content.

335 4.2. Melts

336 Because of the lack of long-range order in silicate melts (or fluids), the variation of $\text{Fe}^{3+}/\text{Fe}^{2+}$ is unbound
 337 by stoichiometry and can vary freely. The ratio of ferrous to ferric iron in silicate liquids can be
 338 understood quantitatively by considering the homogeneous equilibrium:



340 The equilibrium constant of this reaction is:

$$341 \quad K^* = \frac{a(\text{Fe}^{2+} \text{O})f(\text{O}_2)^{1/4}}{a(\text{Fe}^{3+} \text{O}_{1.5})}. \quad (17)$$

342 Where a refers to the activity of the iron oxide component dissolved in the liquid and K^* accounts for
343 their possible deviations from the ideal case (K). Written in terms of $\text{Fe}^{3+}/\Sigma\text{Fe}$:

$$344 \quad \frac{X\text{Fe}^{3+}\text{O}_{1.5}}{\Sigma\text{Fe}} = \frac{1}{1 + 10^{\left(-\frac{1}{4}\log f(\text{O}_2) + \log K - \log \frac{\gamma\text{FeO}}{\gamma\text{FeO}_{1.5}}\right)}}. \quad (18)$$

345 The γFeO and $\gamma\text{FeO}_{1.5}$ refer to the activity coefficients of these species in the silicate melt referenced
346 to the standard states of the pure liquid oxides at the conditions of interest. Using thermodynamic data
347 for reaction (16), Jayasuriya et al. (2004) calculated values of $\gamma\text{FeO} = 1.37$ and $\gamma\text{FeO}_{1.5} = 1.08 \pm 0.33$
348 based on $\text{Fe}^{3+}/\text{Fe}^{2+}$ ratios determined by Mössbauer spectroscopy. These determinations are valid at
349 infinite dilution (which they inferred at 1 wt. % FeO^{T}) in an Anorthite-Diopside eutectic composition
350 at 1400 °C and 1 bar, meaning that iron dissolution in silicate melts is close to ideal. Furthermore, their
351 data showed that $\log(\text{Fe}^{3+}/\text{Fe}^{2+})$ is proportional to $(f\text{O}_2)^{0.245}$, within uncertainty of the theoretical
352 dependence expected from eq. (16), suggestive of no interactions between Fe^{2+} - Fe^{3+} in silicate liquids
353 as a function of $f\text{O}_2$. This hypothesis, that $\frac{\gamma\text{FeO}}{\gamma\text{FeO}_{1.5}}$ is independent of $f\text{O}_2$ for a fixed composition, was later
354 confirmed by Berry et al. (2018) for a natural MORB composition with higher quantities of iron (10 wt.
355 % FeO^{T}).

356 By contrast, $\frac{\gamma\text{FeO}}{\gamma\text{FeO}_{1.5}}$ is readily affected by silicate composition. Dickenson and Hess (1986) show that
357 potassium stabilises tetrahedrally-co-ordinated ferric iron by charge balance. Recent work by Borisov
358 et al. (2017) illustrates that this stabilisation occurs inversely proportional to their bond valence in
359 silicate melts (e.g. Farges et al. 2004) whereas Al competes with Fe^{3+} for tetrahedral sites. This effect
360 is manifest in the higher $\text{Fe}^{3+}/\Sigma\text{Fe}$ in $(\text{Na,K})_2\text{Si}_3\text{O}_7$ silicate melts (Knipping et al. 2015) relative to alkali-
361 poor MORB compositions (Berry et al. 2018) at the same $f\text{O}_2$.

362 The effect of composition on $\text{Fe}^{3+}/\Sigma\text{Fe}$ is evident in the study of Dauphas et al. (2014), the first to
363 combine quantification of X-Ray Absorption Near-Edge Structure (XANES) spectra to determine the
364 redox ratio of glasses with NRIXS spectra to calculate Fe-O force constants. They analysed glass of
365 four different compositions corresponding to basaltic, andesitic, dacitic and rhyolitic liquids melted at
366 1550°C and 1 bar. Notably, the rhyolitic glass has relatively higher $\text{Fe}^{3+}/\Sigma\text{Fe}$ than the more mafic
367 compositions at the same $f\text{O}_2$. While tempting to correlate this shift with silica content, Borisov and
368 McCammon (2010) show that increasing silica results in decreases in $\text{Fe}^{3+}/\Sigma\text{Fe}$ up to 60% SiO_2 , all else
369 being equal, suggestive instead of the role of alkali metals in stabilising tetrahedrally-co-ordinated Fe^{3+} .

370 Dauphas et al. (2014) report an increase in the Fe-O force constant from 199 ± 15 N/m in Fe^{2+} -bearing
371 mafic-intermediate composition, which they extrapolate to 351 ± 29 N/m for $\text{Fe}^{3+}/\Sigma\text{Fe} = 1$ (Fig. 3).

372 Independently of fO_2 , the rhyolitic composition is displaced to higher Fe-O force constants for a given
 373 $Fe^{3+}/\sum Fe$, 240 ± 13 N/m ($Fe^{3+}/\sum Fe = 0$) and 385 ± 24 ($Fe^{3+}/\sum Fe = 1$). This distinction therefore likely
 374 reflects the greater proportion of IV-fold co-ordinated Fe^{3+} in rhyolitic compositions relative to more
 375 basic melts. Although ferrous and ferric iron in basaltic glasses have co-ordination numbers close to V
 376 (though this may be through a combination of IV- and VI-fold rather than V-fold itself), ferric iron
 377 tends to be in slightly lower co-ordination environments than does ferrous iron (Wilke et al. 2007;
 378 Knipping et al. 2015). In both cases, the addition of alkalis stabilises tetrahedrally co-ordinated iron,
 379 the effect being more pronounced for Fe^{3+} (Jackson et al. 2005b; Knipping et al. 2015; Borisov et al.
 380 2017), again inversely proportional to their bond valence ($Rb^+ > K^+ > Na^+ > Li^+$).

381 The relative compressibility of oxide components in silicate melts leads to structural changes as a
 382 function of pressure (e.g., Kress and Carmichael 1991) that can affect isotopic fractionation (section
 383 2.0). At equilibrium, differences in molar volumes (\bar{V}) of the FeO and $FeO_{1.5}$ components with pressure
 384 (P) impact upon their stability, with the resultant change in Gibbs Free Energy of formation (ΔG^o)
 385 described by:

$$386 \quad \Delta G_{(15), T, P}^o = \Delta G_{(15), T, 1 \text{ bar}}^o + \int_{1 \text{ bar}}^P \Delta \bar{V}_{T, P} dP, (19)$$

387 and, with the relation $\Delta G = -RT \ln K$, the ferric-ferrous ratio is given by:

$$388 \quad \ln \left(\frac{X_{FeO_{1.5}}}{X_{FeO}} \right) = - \left(\frac{\Delta G_{(15), T, 1 \text{ bar}}^o + \int_{1 \text{ bar}}^P \Delta \bar{V}_{T, P} dP}{RT} \right) - \ln \left(\frac{\gamma_{FeO_{1.5}}}{\gamma_{FeO}} \right) + \frac{1}{4} \ln fO_2. (20)$$

389 The volume change for eq. (16) at 1 bar is negative, such that FeO would be expected to be stabilised
 390 with respect to $FeO_{1.5}$ with increasing pressure at constant relative fO_2 , assuming no change in their
 391 molar volumes. Calculations of iron redox state by Mössbauer and XANES spectra for iron in andesitic
 392 melts at the Ru-RuO₂ oxygen buffer as a function of pressure bear out this prediction, and show
 393 increasing Fe^{2+}/Fe^{3+} ratios up to 7 GPa (O'Neill et al. 2006; Zhang et al. 2017). This tendency was
 394 modelled using a Murnaghan equation of state with molar volumes from Lange and Carmichael (1987)
 395 and bulk moduli of 30.3 GPa and 16.6 GPa for FeO and $FeO_{1.5}$, respectively (Kress and Carmichael,
 396 1991). Zhang et al. (2017) recognised a densification of the FeO component by a progressive shift in
 397 average iron co-ordination number from 5.5 to 6 over this pressure range, whereas that of $FeO_{1.5}$
 398 remained constant at ≈ 5.3 . However, higher pressure experiments show that the trend of increasing
 399 Fe^{2+}/Fe^{3+} is reversed between 7 and 15 GPa (Armstrong et al. 2017) with Fe^{2+}/Fe^{3+} decreasing thereafter
 400 up to 23 GPa, suggesting ferric iron also transitions to higher co-ordination numbers above 15 GPa.

401 Although co-ordination number increases with pressure, the associated bond stiffening (recalling the
 402 inverse proportionality of volume and vibrational frequency, eq. (8)) results in considerable increases
 403 in $\langle Fe-O \rangle$ force constants in silicate glasses (Liu et al. 2017). At ambient pressure, K_{Fe-O} in Fe^{3+} -free
 404 basaltic glass is ≈ 190 N/m (Fig. 3; Dauphas et al. 2014) whereas it reaches 355 N/m at 65.4 GPa (Fig.

405 4; Liu et al. 2017); equivalent to the effect of quantitative substitution of ferrous for ferric iron at 1 bar.
406 The determined gradient, dK_{Fe-O}/dP , shows two regimes, 0 – 25.8 GPa; $dK_{Fe-O}/dP = 1.22 \pm 0.25$
407 N/m/GPa and 35.1 – 65.4 GPa; $dK_{Fe-O}/dP = 1.81 \pm 0.10$ N/m/GPa, with a discontinuous jump between
408 them (Fig. 4). Therefore, despite evidence for a gradual increase in FeO co-ordination number in silicate
409 glasses under conditions that are relevant to partial melting in the upper mantle (< 7 GPa, Zhang et al.
410 2017), this structural change induces little- or no increase in K_{Fe-O} . By contrast, the step-wise increase
411 in K_{Fe-O} from ≈ 220 N/m to ≈ 300 N/m between 25 – 35 GPa coincides with pronounced densification in
412 basaltic melts, inferred to be caused by the passage of Si from tetrahedral to octahedral co-ordination
413 (Sanloup et al. 2013). Therefore, bulk structural changes in the melt may be more effective in modifying
414 Fe-O force constants than are changes in local bonding environment.

415 4.3. Fluids

416 The compositional parameter space for fluids is larger than that for silicate melts, in which most
417 components are dissolved as oxide species. By contrast, metals can be complexed by Cl-, C-, S- and
418 OH ligands in geologically-relevant fluids (see Burnham 1979; Candela 1989; Manning 2004; Richards
419 2011 for summaries of fluid compositions in arc magmatic and hydrothermal systems). Magmatic fluids
420 are predominantly aqueous, with dissolved components ranging from 17 – 83% (Manning 2004), which
421 are broadly correlative with the P - T conditions at which the fluid equilibrated. Low temperature fluids
422 have metal-bearing species dominated by alkali-chloride complexes (NaCl, KCl), in addition to HCl
423 and SO₂ as other major volatiles (*e.g.*, Richards 2011). The dissolution of Si becomes important at
424 higher temperatures as the composition of the fluid-rock system approaches supercritical behaviour,
425 which occurs at 1.5 GPa and 700°C in the system albite-H₂O (Manning, 2004).

426 Iron, like the alkali metals, likely dissolves as Cl-bearing species in hydrothermal fluids, as evidenced
427 by its strong solubility in Cl-rich fluids (*e.g.*, Kwak et al. 1986). It is expected to be predominantly
428 ferrous; the stability of ferric chloride species are much lower (Testemale et al. 2009; Saunier et al.
429 2011) except during dissolution under very oxidising conditions (*e.g.*, with hematite; Brugger et al.
430 2016). Spectroscopic techniques that have been employed to probe speciation in acidic chloride
431 solutions for a range of Cl molalities from 0.5 to 12 up to 450 °C suggest the presence of higher-order
432 complexes, with the predominance of FeCl₄²⁻ as the dominant Fe-bearing species (Testemale et al.
433 2009). By contrast, speciation of Fe in fluids at relevant P - T conditions (up to 650 °C, 2 kbar; Chou and
434 Eugster 1977; Boctor et al. 1980; Fein et al. 1992) is largely informed by the stoichiometry of mineral
435 dissolution reactions. Iron solubility in fluids is expected to be influenced by temperature, pressure, pH
436 and by the presence of chlorine. The data of Chou and Eugster (1977) on magnetite solubility in HCl
437 solutions conform to a stoichiometry with FeCl₂ as the stable fluid species, whose solubility is given as
438 $\log m(\text{FeCl}_2) = 6887/T(\text{K}) - 8.44^2$. Ding & Seyfried (1992) experiments showed that (FeCl)⁺ and

² m refers to the molality, in mol/kg; whereas mmolal refers to mmol/kg

439 particularly FeCl_2 are the dominant Fe species in aqueous fluids at the hematite-magnetite buffer and
 440 up to 450 °C and 0.3 to 0.5 kbar. The solubility of Fe increases drastically with increasing NaCl
 441 concentrations, passing from 0.369 mmolal of Fe at 350°C and 29.1 mmolal of Na to 1.285 mmolal of
 442 Fe at 500°C and 1233 mmolal of Na (see also Fig. 12 in Testemale et al., 2009). These authors also
 443 observed FeCl_2 as the dominant species with increasing temperatures. Indeed, thermodynamic
 444 calculations at high pressure and temperature (630-660 °C and 2 GPa) show that Fe is mobile in slab-
 445 derived fluids as FeCl_2 during antigorite breakdown (Debret & Sverjensky, 2017). It should be noted
 446 that the complexation of Fe^{2+} with sulfate, carbonate or silica was not considered in these
 447 thermodynamic models due to the absence of thermodynamic data; although this is not proof that these
 448 species do not exist. Furthermore, even though Fe^{3+} -complexes were included, they were found to be
 449 unimportant at the investigated conditions.

450 These studies all point to the predominance of FeCl_2 , particularly at high temperatures. Nevertheless,
 451 there is a dearth of experimental studies at conditions relevant to that of subduction zone magmatism
 452 or high-temperature ore-forming hydrothermal fluids (> 800 °C). One of the few are the magnetite
 453 solubility experiments of Simon et al. (2004) who also presumed FeCl_2 as the stable species and
 454 measured up to 7.3 wt. % iron in the fluid phase at high NaCl molalities. Sanchez-Valle et al. (2017)
 455 recorded XANES spectra of chlorinated-aqueous fluids equilibrated with Fe-bearing minerals in a
 456 diamond anvil cell at 2.5 GPa and 800°C. Their results imply the transport of Fe with $(\text{Fe}^{2+}\text{Cl}_x)^{2-x}$
 457 stoichiometries, with the stability of Fe^{3+} -bearing chloride species decreasing with increasing
 458 temperature.

459 In a series of studies, Hill and co-workers calculated and measured experimentally the isotopic
 460 fractionation between a variety of iron chlor-aquo species at ambient temperatures (Hill and Schauble
 461 2008; Hill et al. 2009, 2010). These studies show several trends at 298 K:

- 462 1) The iron isotope fractionation factor and calculated force constants decrease with increasing
 463 chlorinity. Specifically, $10^3 \ln \beta^{56/54}\text{Fe} (\text{FeCl}_x(\text{H}_2\text{O})_{6-x})^{3-x}$ is 9.41, 8.54, 8.10, 7.13 and 7.14 for x
 464 = 0, 1, 2, 3 and 4, respectively.
- 465 2) In the equivalent ferrous-iron bearing system, the species have $10^3 \ln \beta^{56/54}\text{Fe}(\text{FeCl}_x(\text{H}_2\text{O})_{6-x})^{2-x}$
 466 of 6.39, 5.98, and 5.91 for $x = 0, 1, \text{ and } 2$, respectively.
- 467 3) Regardless of the basis set used for the *ab-initio* calculations, the fractionation factor $10^3 \ln \alpha_{3+}$
 468 $_{2+} \approx 3\%$.

469 Fujii et al. (2014) calculated β factors for a host of aqueous, ferric- and ferrous iron-bearing species
 470 (Fig. 5). Though there are minor differences in $10^3 \ln \beta^{56/54}\text{Fe}$ among species of a given Fe oxidation
 471 state, these differences become small (<0.3 ‰) by 573 K. Invariably, species with chloride ligands are
 472 the lightest among other species studied, particularly compared to PO_4^{3-} , OH^- and SO_4^{2-} which are
 473 stronger-field ligands and therefore concentrate the heavier isotopes (Fig. 5). A similar order can be

474 observed among Fe³⁺-bearing compounds (Fig. 5). As per the study of Hill et al. (2010), the isotopic
 475 fractionation between Fe²⁺ and Fe³⁺-bearing species is most marked. At 573 K, the value of
 476 $10^3 \ln \beta^{56/54} \text{Fe}_{3+-2+} \approx 0.90 \text{ ‰}$, suggesting iron isotopes should be a powerful discriminant of the oxidation
 477 state of iron in fluids, even at high temperatures, but not between different ligands for the same oxidation
 478 state of iron.

479 Iron isotope compositions of chlorine-bearing fluids relevant to hydrothermal systems (300 – 350 °C)
 480 were explored for the systems fluid-pyrite (Syverson et al. 2013) and fluid-chalcopyrite (Syverson et
 481 al. 2017). Solutions equilibrated with pyrite contained $\approx 10 \text{ mmol/kg Fe}^{2+}$ and $\approx 1000 \text{ mmol/kg Na}$, and,
 482 at low pH (≈ 3 at 350°C) and 500 bar, $\text{Fe}(\text{H}_2\text{O})^{2+}$ was calculated to have been stable, and defined a
 483 fractionation factor $10^3 \ln \alpha^{(57/54)\text{Fe}_{\text{pyr-fluid}}} = +1.49 \pm 0.44 \text{ ‰}$. This gives a force constant for $\text{Fe}(\text{H}_2\text{O})^{2+}$
 484 of $\approx 150 \text{ N/m}$ (given that of pyrite is $\approx 280 \text{ N/m}$; Blanchard et al. 2009). Under the same conditions, the
 485 fractionation between chalcopyrite and fluid, $10^3 \ln \alpha^{(57/54)\text{Fe}_{\text{ccp-fluid}}} = +0.09 \pm 0.17 \text{ ‰}$ is negligible within
 486 uncertainty (Syverson et al. 2017). At 300 °C and NaCl-HCl±FeCl₂ fluids, dissolution/precipitation of
 487 hematite yielded $10^3 \ln \alpha^{(57/54)\text{Fe}_{\text{hem-fluid}}} = +0.54 \pm 0.15 \text{ ‰}$ in which the fluid species was likely FeCl₂⁰(aq)
 488 or FeCl⁺, however no fractionation was observed at 450 °C and 600 bar, nor at 200 °C, where the fluid
 489 phase was inferred to be dominated by Fe³⁺-bearing aqueous species (Saunier et al. 2011). Nevertheless,
 490 this sequence of isotopic fractionation ($\delta^{57}\text{Fe}_{\text{pyr}} > \delta^{57}\text{Fe}_{\text{hem}} > \delta^{57}\text{Fe}_{\text{mag}} > \delta^{57}\text{Fe}_{\text{ccp}} \geq \delta^{57}\text{Fe}_{\text{fluid}}$) is borne out
 491 in measurements of hydrothermally-precipitated ore phases (Wawryk and Foden 2015, 2017; Li et al.
 492 2018). Higher temperature experiments carried out at 800°C and 10 kbar by Sossi and O'Neill (2017)
 493 found strong isotopic fractionation between FeCl₂·4H₂O fluid and Fe³⁺-rich minerals (namely
 494 magnetite), where $10^3 \ln \alpha^{(57/54)\text{Fe}_{\text{mag-fluid}}} = +0.44 \pm 0.01 \text{ ‰}$. By contrast, ^{VI}Fe²⁺-bearing minerals
 495 (fayalite, ilmenite) had similar iron isotope compositions to the fluid, and almandine garnet was lighter
 496 still, at $10^3 \ln \alpha^{(57/54)\text{Fe}_{\text{alm-fluid}}} = -0.14 \pm 0.03 \text{ ‰}$, which gives the iron force constant for FeCl₂⁰ in the fluid
 497 of 175 N/m. This compares well with force constants of 153 – 186 N/m for FeCl₂(H₂O)₄ calculated in
 498 Hill et al. (2010) depending on the DFT basis set used, their Table A1.

499 5.0. Effect of redox processes in influencing iron isotope fractionation in natural systems

500 5.1. Magmatic processes

501 5.1.1. Partial Melting

502 Partial melting is the process that describes the incomplete transformation of a solid(s) to a liquid phase.
 503 In terrestrial magmatic settings, this process can occur in both the crust and mantle. Should liquid-solid
 504 segregation occur, this process has the capacity to impart isotopic fractionation on its constituent phases.

505 Though early studies considered that the compositions of mantle peridotites and basaltic rocks were
 506 indistinguishable (e.g. Zhu et al. 2001; Beard et al. 2003a) leading to the development of the concept
 507 of 'mean mafic Earth' with $\delta^{57}\text{Fe} = +0.10 \pm 0.03 \text{ ‰}$, later, higher-precision studies soon overturned this

508 perception. In particular, two studies, Williams et al. (2005) and Weyer and Ionov (2007) presented an
 509 extensive number of analyses of whole rock peridotites and, in the case of the former, their constituent
 510 minerals. The conclusion from both of these works was that peridotitic rocks were isotopically lighter
 511 ($\delta^{57}\text{Fe} = +0.03 \pm 0.05 \text{ ‰}$ at $\text{Mg\#} = 0.894$, that of fertile mantle) than their basaltic counterparts and
 512 secondly, that partial melting of the mantle could induce resolvable isotopic fractionation in which the
 513 residual peridotite composition would tend to lighter isotopic values with progressive extraction of
 514 heavier basaltic melt. Weyer and Ionov (2007) assigned bulk peridotite-liquid fractionation factors that
 515 fit arrays of $\delta^{57}\text{Fe}$ vs. Mg\# (molar $\text{Mg}/(\text{Mg}+\text{Fe}^{2+})$) to quantify this effect, finding $10^3 \ln \alpha(^{57/54}\text{Fe}_{\text{mantle-melt}})$
 516 $= -0.1$ to -0.3 ‰ . These fractionation factors were also used to fit the observation of the isotopically
 517 heavy ($\delta^{57}\text{Fe} = +0.15 \text{ ‰}$) compositions of basaltic rocks measured to that stage.

518 As recognised by Williams et al. (2005) and Weyer and Ionov (2007), iron isotope fractionation arises
 519 mechanistically from the incompatibility of Fe^{3+} relative to Fe^{2+} , reflected in the higher $\text{Fe}^{3+}/\sum\text{Fe}$ of
 520 MORB glasses (0.10 ± 0.02 ; Berry et al. 2018) relative to peridotites (0.037 , Canil et al. 1994).
 521 Clinopyroxene is the major contributor to partial melting at low pressures ($<3 \text{ GPa}$) (e.g., Hirschmann
 522 et al. 1999), and $D(\text{Fe}^{2+})/D(\text{Fe}^{3+})^3 \approx 10$, where $D(\text{Fe}^{2+}) \approx 1$ (e.g., Mallmann and O'Neill 2009; Davis et
 523 al. 2013). Therefore, during melt extraction, the modal olivine content increases and, as it contains less
 524 ferric iron than ortho- and particularly clinopyroxene or spinel (Canil and O'Neill 1996), tends to
 525 concentrate the lighter isotopes. Dauphas et al. (2009) developed a melting model predicated on the
 526 difference of $\text{Fe}^{3+}/\text{Fe}^{2+}$ ratios of the mantle source and the partial melt. As ferric iron behaves as an
 527 incompatible element, the extent of isotopic fractionation is highest in the melt at low degrees of
 528 melting, a feature also attributable to the mass balance considerations (i.e., the 'lever rule'). However,
 529 this treatment implicitly neglected the effect of co-ordination environment, whose isotopic effect was
 530 unconstrained until the study of Dauphas et al. (2014), whose measurement of Fe-O force constants in
 531 magmatic glasses revealed a preference for the heavier isotopes in lower co-ordination environments
 532 (section 4.2.). With this knowledge, combined with $K_{\text{Fe-O}}$ of mantle minerals, Sossi and O'Neill (2017)
 533 were able to build self-consistent modal and non-modal melting equations based on the mass balance
 534 equations of Shaw (1970), re-cast in terms of isotopic fractionation between phases 1 and 2:

$$535 \quad \frac{C_l^i}{C_o^i} = \frac{1}{\left(\left(D_{1-2}^i \alpha^i E_{1-2} \right) + F \left(1 - P \left(D_{1-2}^i \alpha^i E_{1-2} \right) \right) \right)}, \quad (21)$$

536 where C_l^i and C_o^i denote the concentration of isotope i of element E in the liquid and bulk, respectively,
 537 F is the melt fraction and P the product of a phase's melting reaction coefficient and elemental D

³ The elemental partition coefficient, denoted 'D', is given by the ratio of the concentration of the element in a solid phase with respect to that in the liquid phase.

538 summed over each phase. Solutions are found for the concentration of each isotope, and hence the
 539 resulting isotopic composition of the liquid is:

$$540 \quad 10^3 \ln \left(\frac{C_l^i}{C_l^j} \right) = \delta^i E. \quad (22)$$

541 The above equations can be applied to any isotope system. For iron, the crucial free variable, D_{1-2}^i , is
 542 controlled by the temperature and difference in iron force constants between phases 1 and 2 (mineral
 543 and melt):

$$544 \quad D_{Min-Melt}^{54+nFe} = \left(D_{Min-Melt}^{54Fe} \right) e^{\left(\frac{1435n(K_{Fe-o}^{Min} - K_{Fe-o}^{Melt})}{T^2} \right)}. \quad (23)$$

545 Here, $n = 2$ ($^{56/54}Fe$) or 3 ($^{57/54}Fe$). The force constant for each phase is given in the form:

$$546 \quad K_{Fe-o} = a \times \frac{Fe^{3+}}{\Sigma Fe} + b \quad (24)$$

547 where a describes the slope of the dependence of the force constant with the $Fe^{3+}/\Sigma Fe$, and b the y -
 548 intercept, which depends on co-ordination ($VIII < VI < IV$). Values of constant a and b can be calculated
 549 from Figs. (1 - 3), and yield $a = 125$ and $b_{VIII} = 145$ N/m, $b_{VI} = 185$ N/m and $b_{IV} = 225$ N/m.

550 Systematics of iron isotope fractionation applying this partial melting model are summarised in Figs.
 551 6a and b. As in the models presented in Dauphas et al. (2009), iron isotope fractionation between the
 552 melt and its source is inversely proportion to the melt fraction (Fig. 6a), as the $Fe^{3+}/\Sigma Fe$ of the melt is
 553 maximised at low F due to the relative incompatibility of ferric iron. Independent of this effect is the
 554 modal mineralogy of the source; as the modal abundance of garnet increases at the expense of olivine
 555 (e.g., via increasing pressure or in a bimineralic eclogite), the fractionation factor increases due to the
 556 retention of the light isotopes in its VIII-fold sites.

557 This mineralogical control on the extent of iron isotope fractionation can account for the isotopic
 558 differences between mantle peridotites, MORBs and OIBs. The iron isotope variations observed in
 559 mantle peridotites are more scattered than those in basaltic rocks. Studies reporting analyses of
 560 peridotitic or ultramafic lithologies include (Poitrasson et al. 2004, 2013; Williams et al. 2004, 2005,
 561 2009; Weyer et al. 2005; Weyer and Ionov 2007; Zhao et al. 2010, 2012, 2017; Huang et al. 2011;
 562 Craddock et al. 2013; Sossi et al. 2016) and were summarised by Sossi et al. (2016), who filtered the
 563 data for unmetasomatised, unaltered, and fertile peridotites. This procedure greatly reduced data
 564 variability enabling a 2SE uncertainty to be taken of 60 peridotite analyses that yielded $\delta^{57}Fe = +0.05$
 565 ± 0.01 ‰ for the value of fertile mantle. These authors noted that significant iron isotope fractionation
 566 in fresh, unmetasomatised peridotites was not evident until reaching $Mg\#s > 0.91$, reflecting the
 567 retention of the bulk of the iron budget in the peridotite.

568 Relative to ultramafic rocks, oceanic basalts almost exclusively preserve heavier iron isotope
569 compositions (Weyer and Ionov 2007). Nevertheless, data for oceanic basalts remained sporadic until
570 the study of Teng et al. (2013), in which 93 iron isotope analyses of basaltic rocks were presented,
571 comprising 43 MORBs, whereas the remainder were OIBs from the Society Islands, the Cook-Austral
572 chain and Hawai'i. The isotopic composition of MORB gave a mean value of $\delta^{57}\text{Fe} = 0.15 \pm 0.01 \text{ ‰}$
573 (2SE, $n = 43$), some 0.1 ‰ heavier than fertile mantle. Considering that the maximum iron isotope
574 fractionation permitted during melting of peridotite in the spinel facies is 0.05 ‰ at FMQ (Fig. 6a), this
575 poses a conundrum for the derivation of MORB from peridotitic upper mantle (see discussion in
576 Dauphas et al. 2014). However, as noted by Sossi et al. (2016), MORBs have Mg#s that are too low
577 ($0.54 < \text{Mg\#} < 0.68$) to have been in equilibrium with Fo₉₀ mantle olivine, which, since $K_D^{\text{Fe-Mg}}$
578 ($[\text{Fe}^{2+}/\text{Mg}]_{\text{Ol}}/[\text{Fe}^{2+}/\text{Mg}]_{\text{Melt}}$) is equal to ≈ 0.3 (Toplis 2005), should produce melts with Mg# ≈ 0.74
579 (compositional effects on $K_D^{\text{Fe-Mg}}$ broadly cancel such that the use of a single value introduces minimal
580 uncertainty). In this scenario, the low-pressure evolution of MORB magmas during decompression
581 expands the olivine phase volume (Kinzler and Grove 1992) and light iron isotopes preferentially
582 sequestered into olivine, resulting in heavier values than could be accounted for by single-stage melt
583 extraction. Correction of the iron isotope composition of MORB to a fictive primary melt composition
584 with Mg# ≈ 0.74 yields $\delta^{57}\text{Fe} = 0.10 \text{ ‰}$ (Sossi et al. 2016) that can be reconciled with partial melting.
585 Additional possibilities, including diffusive effects during partial melting (*e.g.*, Weyer and Ionov 2007;
586 Poitrasson et al. 2013; Su et al. 2015), may also become important in fractional melting regimes where
587 melt parcels and residual mantle equilibrate only at infinitesimally small increments (see Asimow et al.
588 1997). Here, preferential transport of the lighter iron isotopes into peridotite minerals during ascent,
589 due to its faster diffusivity, would lead to heavier isotopic compositions than predicted by equilibrium
590 fractionation factors.

591 With respect to MORBs, OIBs are frequently (though not always; Peters et al. 2019) higher in $\delta^{57}\text{Fe}$
592 (Teng et al. 2013), a tendency that was highlighted in the data of Williams and Bizimis (2014) and
593 Konter et al. (2016) on MgO-rich pyroxenites and OIBs from Hawai'i and Samoa, respectively. In these
594 samples, whose Mg# reaches 0.69, $\delta^{57}\text{Fe}$ can extend to +0.45 ‰, up to 0.4 ‰ heavier than recent
595 estimates for fertile mantle peridotite. All things being equal, OIBs should be heavier than MORBs by
596 virtue of the lower degrees of partial melting involved in their genesis (section 5.1.1., Fig. 6).
597 Nevertheless, this offset is greater than can be produced by degree of melting alone, and the combination
598 of isotopically heavy iron and high Mg# requires additional source-related melting controls. Both
599 studies argue for the presence of pyroxenite in the source, which has the dual effect of i) increasing the
600 $\delta^{57}\text{Fe}$ of the source (pyroxenites from Oahu, Hawai'i have $\delta^{57}\text{Fe}$ between +0.10 and +0.27 ‰, Williams
601 and Bizimis, 2014) and ii) enhancing iron isotope fractionation during partial melting. This second point
602 was quantified in Sossi and O'Neill (2017) who demonstrated that such heavy values were difficult to
603 create during melting of mantle peridotite, and instead required a high fraction of garnet in the source

604 that simultaneously acted as a sink for light iron isotopes (see Fig. 6a) and increased the Gd/Yb ratio of
605 the basalts (Fig. 7).

606 The expected effect of source oxidation is to increase the iron isotope fractionation observed in products
607 of partial melting (Dauphas et al. 2009; Fig. 6b). Although the consensus is that arc magmas are more
608 oxidised than those from oceanic settings (MORBs and OIBs; see Carmichael 1991; Kelley and Cottrell
609 2009), conjecture still abounds as to whether the sources of arc magmas are more oxidised than their
610 equivalents under mid-ocean ridges or ocean islands (Lee et al. 2005; Mallmann and O'Neill 2009). In
611 this scenario, the higher oxygen fugacity of arc magmas could be acquired after segregation from their
612 mantle sources, by fractional crystallisation or degassing of reduced species, such as H₂ or CH₄ (Mathez
613 1984). The sensitivity of iron isotopes to the redox state of iron may in turn be able to distinguish
614 between these two hypotheses.

615 Should the sources of arc magmas be more oxidised, then the mechanics of iron isotope fractionation
616 would predict an iron isotope composition heavier than oceanic basalts. Analyses of arc magmas were,
617 until recently, surprisingly sparse, restricted to studies of back-arc basalts (Nebel et al. 2013; 2018) and
618 two arcs; New Britain (Dauphas et al. 2009) and the sediment-rich Banda (Nebel et al. 2015) prior to
619 the extensive dataset comprising 130 arc magmas of Foden et al. (2018). These authors discovered,
620 contrary to expectations, that arc magmas have systematically lighter iron isotope composition relative
621 to MORBs, extending to values even lighter than fertile mantle peridotites, around -0.15 ‰ in
622 Avachinsky, Klyuchevskoy and Ploskiy volcanoes of the Kamchatka arc (Foden et al. 2018). This result
623 has two important implications. Firstly, if the sources of arc magmas are indeed more oxidised than
624 ambient mantle, then iron itself cannot be the cause of this oxidation. Rather, the role of S⁶⁺ as the
625 oxidising agent for arc magmas is supported by quantitative calculations of the redox budget of
626 subduction zones (Evans and Tomkins 2011), largely due to its efficiency in oxidising iron via an 8-
627 electron transition from sulfate to sulfide:



629 This means 8 moles of Fe are oxidised for every mole of S, which equates to 1.8 wt. % FeO per 1000
630 ppm S; the S content of MORB, though those of arc magmas are even higher (Wallace and Edmonds
631 2011). This comes about due to the higher solubility of sulfur in silicate melts at anhydrite saturation
632 with respect to sulfide saturation (O'Neill and Mavrogenes 2002; Li and Ripley 2009; Smythe et al.
633 2017). Alternatively, the idea that the oxygen fugacities of arc magma sources are similar to ambient
634 mantle stands. In either case, iron isotopes show no evidence for the oxidation of arc magma sources.

635 Secondly, the observation that arc magmas are *lighter* than oceanic basalts begs explanation. Nebel et
636 al. (2015) argued that the isotopically light sources could be generated by the prior extraction of melt
637 from peridotite sources, which are known to be more refractory than ambient mantle on the basis of

638 lower abundances of incompatible high field strength elements (Nb, Ti) in arc magmas. These elements
 639 behave conservatively during slab fluid transfer to the mantle wedge and represent the composition of
 640 mantle wedge peridotite (Woodhead et al. 1993). Degrees of partial melting needed to explain the
 641 degree of isotopic fractionation is close to 30%, which are observed in xenoliths from the Bismarck arc
 642 (Bénard et al. 2018). However, Foden et al. (2018) asserted that values as low as -0.15 ‰ cannot be
 643 produced by melt depletion alone, and considered additional scenarios. In particular, diffusive stripping
 644 of lighter isotopes in preference to their heavier counterparts was cited as a mechanism to promote light
 645 isotope compositions in partial melts. As discussed in section 4.3., the iron isotope composition of
 646 aqueous fluids are light provided the speciation of iron is dominated by Fe²⁺-bearing species,
 647 particularly FeCl₂, as inferred from the measurements of Sanchez-Valle et al. (2017). However, it
 648 remains uncertain as to whether the Fe content of these fluids is high enough to shift the iron isotope
 649 composition of the mantle wedge (Ayers et al. 1997; see also section 5.2.3). Indeed, supra-subduction
 650 zone ophiolitic peridotites, despite their high degree of depletion ($\approx 25 - 35\%$) and re-enrichment with
 651 subduction zone fluids, resulting in a distinctive ‘U-shape’ REE pattern, are not systematically lighter
 652 than abyssal peridotites (Su et al. 2015; Zhang et al. 2019). Although certain samples extend to the
 653 requisite light values ($\delta^{57}\text{Fe} \approx -0.15\text{‰}$), this variation is, at best, weakly-dependent on proxies for
 654 degree of melt extraction (Mg#, Cr# in spinel or clinopyroxene) or fluid addition (Ba/Th, Ba/La). By
 655 contrast, Turner et al. (2018) observe a positive correlation between $\delta^{57}\text{Fe}$ and $\delta^7\text{Li}$ to very low values
 656 (-0.46 ‰ and -1.78 ‰, respectively), pointing to fluid addition and/or diffusive processes, though the
 657 primary mechanism for inducing these variations remains uncertain. Further studies of sub-arc mantle
 658 peridotites are required to evaluate the degree to which these process are liable to affect their iron
 659 isotopes compositions locally.

660 On a global scale, Foden et al. (2018) recognised a negative correlation between the iron isotope
 661 composition of global arc magmas and the thermal parameter (ϕ):

$$662 \quad \phi = age \times \sin \theta u, \quad (26)$$

663 the product of slab age and vertical descent velocity, u , where θ is the dip angle (Kirby et al. 1996)
 664 (Fig. 8). Subducting slabs that are old and cold tend to descend at faster rates, such that they do not
 665 thermally equilibrate as much with surrounding mantle, and slab geotherms are too cold to permit slab
 666 melting. By contrast, hotter slabs descend more slowly due to their thermal buoyancy, and hence heat
 667 up to greater extents during their protracted residence time in the mantle, allowing partial melting of
 668 the slab. Foden et al. (2018) also suggested that the mantle wedge peridotite in longer-lived and
 669 therefore colder subduction zones remained trapped in the sub-arc mantle by convective ‘Richter rolls’
 670 (Davies et al. 2016), subjecting the same mantle to continual melt-extraction and fluid ingress, which
 671 may have been partially kinetic in nature (see also Zhao et al. 2012), resulting in isotopically light arc
 672 magma sources. Alternatively, on the basis of the similarity in iron isotope compositions of sub-arc and

673 convecting mantle, Zhang et al. (2019) propose that redox-unbuffered melting of arc sources may
674 account for their lighter composition than MORB, yet this does not address the very light isotope
675 signatures observed in magmas from high ϕ arcs such as Kamchatka and Samoa.

676 5.1.2. Differentiation

677 Magmatic differentiation comprises the range of processes involving, but not limited to, fractional
678 crystallisation, crustal assimilation, fluid exsolution, Soret diffusion and vapour-phase degassing, all of
679 which have the potential to fractionate iron isotopes by mass transfer.

680 The earliest concerted effort to study the effect of magmatic differentiation on iron isotope fractionation
681 was that of Poitrasson and Freydier (2005), who analysed a collection of granites including peralkaline,
682 metaluminous and peraluminous varieties, broadly corresponding to A-, I- and S-type magmas,
683 respectively (Chappell and White 1974; Frost and Frost 2010). These granitic rocks recorded a near-
684 exponential increase in $\delta^{57}\text{Fe}$ with falling MgO (below 1 wt. %) or rising SiO_2 (above 70 wt. %) contents
685 (their Figs. 5 and 6) relative to the 'mean mafic earth' value of $\delta^{57}\text{Fe} = +0.10 \pm 0.03 \text{ ‰}$ reaching $+0.59$
686 $\pm 0.03 \text{ ‰}$ (Poitrasson and Freydier 2005). In order to explain this monotonic increase, Poitrasson and
687 Freydier (2005) appealed to the exsolution of Fe^{2+} -rich fluids that transported isotopically light iron. A
688 similar trend was observed by Schoenberg and von Blanckenburg (2006), who cited that additional
689 constraints were required to explain the isotopic relationship with SiO_2 content. A fluid-exsolution
690 hypothesis was extended further by (Heimann et al. 2008), who, compiling much of the data available
691 to date (Fig. 9), confirmed the trend of Poitrasson and Freydier (2005) in which silicic igneous rocks
692 exhibited strong positive deviations from mafic igneous rocks above 70 wt. % SiO_2 . These authors
693 considered that the lack of correlation of iron isotope composition with incompatible element
694 concentrations (which can be inverted to yield the fraction of melt remaining) argued against the role
695 of fractional crystallisation in determining iron isotope compositions. The observed inverse correlation
696 between Zr/Hf and $\delta^{57}\text{Fe}$ was taken as evidence for the effect of fluid exsolution, as Heimann et al.
697 (2008) asserted that these trace elements remain little-affected by crystal fractionation (but see Linnen
698 and Keppler 2002). In these highly differentiated rocks, most of the iron is contained in Fe-Ti oxides
699 (specifically magnetite in oxidised granites and rhyolites), and therefore should retain the heavy
700 isotopes, where Heimann et al. (2008) modelled $\Delta^{57}\text{Fe}_{\text{mag-fluid}}$ between $\approx +0.45 \text{ ‰}$ at 700°C and \approx
701 $+0.75 \text{ ‰}$ at 500°C . Because the solubility of FeCl_2 decreases with temperature and isotopic fractionation
702 is proportional to $1/T^2$, the more fractionated granites should preserve the heaviest iron isotope
703 compositions.

704 Contemporaneously, Teng et al. (2008) and Schuessler et al. (2009) published two studies showing
705 unequivocal evidence for the role of crystal-liquid fractionation in controlling iron isotope variations in
706 differentiating magmatic systems. Whole rocks from the Kilauea Iki lava lake, Hawai'i, record
707 progressive enrichment of the heavy isotopes of iron with decreasing MgO, from values close to 0 ‰

708 in olivine cumulates to + 0.3 ‰ in evolved basaltic samples (Teng et al. 2008). Importantly, isotopic
709 fractionation is observed below 70 wt. % SiO₂, in contrast to other differentiating magmatic systems.
710 This variation broadly correlates with the Fe³⁺/ΣFe content of the whole rock, and, more precisely,
711 reflects the incorporation of isotopically light iron into the ^{VI}Fe²⁺ sites of olivine relative to the residual
712 melt, fit with a fractionation factor $10^3 \ln^{57/54} \text{Fe} \alpha_{\text{ol-melt}} = -0.20 \pm 0.10$ ‰. Unlike at Kilauea Iki, isotopic
713 fractionation at the Hekla volcano, Iceland, occurs only around 70 wt. % SiO₂, in line with earlier studies
714 (Schuessler et al. 2009). These authors rejected the hypothesis of fluid exsolution as the cause for this
715 variation, based on the constancy of the isotopes of Li, an element even more fluid-mobile than iron, in
716 the same rocks. Instead, they argued for crystallisation of Ti-rich titanomagnetite, which crystallises as
717 Mag₃₅ at Hekla (Baldrige et al. 1973), in elevating the iron isotope composition in evolved rocks.

718 The absence of iron isotope fractionation below 70 wt. % SiO₂, except for the differentiating sequence
719 of basalts at Kilauea Iki behaved an explanation. The Red Hill intrusion, southern Tasmania, exhibits a
720 vertical continuum of compositions created by in situ fractional crystallisation of a single injection of
721 magma in a closed system (Sossi et al. 2012). Much like the Kilauea Iki lava lake, the iron isotope
722 composition of dolerites from Red Hill increased in δ⁵⁷Fe at high MgO contents, before reaching a
723 maximum near +0.30 ‰ and declining following the crystallisation of magnetite (Mag₉₅), an effect that
724 had been expected, but never observed, on the basis of experimental constraints (Shahar et al. 2008).
725 Thus, iron isotopic evolution for the tholeiitic series mirrored that followed by the liquid line of descent
726 on an AFM (Alkalis-FeO-MgO) diagram, and Sossi et al. (2012) were able to derive fractionation
727 factors; $\Delta^{57}\text{Fe}_{\text{cpx-melt}} = -0.25 \times 10^6/T^2$ and $\Delta^{57}\text{Fe}_{\text{mag-melt}} = +0.20 \times 10^6/T^2$. These authors also pointed out that
728 the differing behaviour of Kilauea Iki and Red Hill on one hand and Hekla on the other could be
729 attributed to the extent to which the differentiating system remained open to oxygen exchange (Fig. 10).
730 Systems that are closed to oxygen exchange, which may be imposed by the formation of chilled
731 margins, have only a finite oxygen budget. Therefore, the early crystallisation Fe²⁺-rich phases increases
732 the Fe³⁺/ΣFe and δ⁵⁷Fe of the melt, prior to the crystallisation of magnetite-rich titanomagnetite, whose
733 high Fe³⁺/ΣFe ratio and hence δ⁵⁷Fe is higher than that of the melt. By contrast, systems open to O₂
734 exchange are buffered at values near FMQ, potentially by chemical and mass exchange with
735 surrounding wall rocks (Carmichael 1967). Here, the Fe³⁺/ΣFe of the melt and minerals remains similar,
736 and they precipitate Ti-rich titanomagnetite, with potentially lower Fe³⁺/ΣFe than the melt, causing an
737 increase in the iron isotope composition of the residual melt.

738 Studies of layered intrusions reveal more complex histories that involve the introduction of several
739 pulses of magma and crystal accumulation that blurs the isotopic signal of the evolving melt(s).
740 However, the conclusion from these studies is that magmatic differentiation does not induce significant
741 isotopic fractionation in the bulk rocks (Chen et al. 2014; Liu et al. 2014; Bilenker et al. 2017),
742 notwithstanding the fact that the individual minerals comprising these rocks can be strongly
743 fractionated. Isotopic fractionation generally occurs in the sequence magnetite > clinopyroxene >

744 olivine > ilmenite, in broad agreement with the hierarchy depicted in section 4.1. Equilibration
745 temperatures of ilmenite-magnetite pairs suggest slow cooling as anticipated for intrusive magmas, and
746 point to sub-solidus re-equilibration as the cause for these disparate isotopic signatures, thereby leaving
747 the composition of the whole rock unaffected.

748 The uniformly heavy iron isotope composition of silicic melts also has its origin in the increased bond
749 strength of iron in these highly polymerised, alkali-rich compositions (section 4.2.), as suggested by
750 Schuessler et al. (2009) and Sossi et al. (2012). This behaviour was conclusively illustrated in the
751 combined NRIXS-XANES study of Dauphas et al. (2014), which showed an increase in Fe–O force
752 constants of felsic melts relative to mafic and intermediate compositions at a given $\text{Fe}^{3+}/\Sigma\text{Fe}$ (see section
753 4.2.). Foden et al. (2015), upon analysing 42 A-, I- and S-type granites, and compiling literature data,
754 found that only the A-type granites, especially the peralkaline ones, that form from protracted
755 crystallisation of basaltic magma (Turner et al. 1992) exhibited heavy iron isotope compositions. As
756 these granites are typically reduced and H_2O - and volatile-poor, their heavy compositions likely reflect
757 extensive crystal-liquid segregation rather than fluid exsolution. More reduced, ilmenite-bearing S-type
758 granites also display a similar isotopic evolution, whereas more oxidised, magnetite-series I-type
759 granites never reach heavy iron isotope compositions, likely due to the combined effect of isotopically
760 light olivine and heavy magnetite in cancelling each other out. This behaviour is evident in evolving
761 magmatic rocks from the Anatahan volcano of the Marianas arc (Williams et al. 2018), in which the
762 effect of magnetite crystallisation is less pronounced than at Red Hill (a change in $\delta^{57}\text{Fe}$ of ≈ 0.15 ‰)
763 after displaying mildly rising iron isotopic values prior to this point. The iron isotopic evolution then
764 increases towards heavier values at very low MgO contents below 2 wt. %, as per other siliceous igneous
765 rocks.

766 Within this framework, recent years have seen a flurry of studies focusing on better understanding the
767 nature of inter-mineral and mineral-melt fractionation in evolved magmatic systems (Du et al. 2017; He
768 et al. 2017; Wu et al. 2017; Xia et al. 2017; Li et al. 2019). These studies argue for the predominant role
769 of fractional crystallisation in producing the heavy $\delta^{57}\text{Fe}$ values of high silica igneous rocks, by a
770 combination of the crystallisation of Ti-rich titanomagnetite and increasing Fe–O bond strength in
771 highly silicic melts with high total alkali/alkaline earth cation ratios (Du et al. 2017; Wu et al. 2017),
772 with residual garnet contributing in peraluminous compositions (He et al. 2017). Noteworthy is the very
773 heavy isotopic composition of plagioclase (Fig. 11), which attests to the preferential incorporation of
774 ferric iron into its structure, as expected on thermodynamic grounds (Lundgaard and Tegner 2004).
775 However, the proportion of total iron hosted in plagioclase is so low so as to be unimportant.

776 5.2. Fluid transfer from mantle to crust

777 High-pressure (HP) metamorphic ophiolites (meta-ophiolites) returned from former subduction zones
778 provide information on deep geochemical processes occurring in subduction zones (Poli and Schmidt

779 2002). They constitute an alternative and complementary way to arc magmas to study the isotopic
780 composition and redox state of the fluids released during slab dehydration and devolatilisation at depth.
781 This is of particular importance for establishing the mass balance of key redox-sensitive elements, such
782 as iron, in subduction zones. However, direct constraints on the redox state and the isotopic evolution
783 of Fe in oceanic lithosphere during subduction remain challenging and the constraints sparse.

784 5.2.1. Altered oceanic lithosphere

785 The subducting slab consists of ultramafic oceanic mantle, the mafic oceanic crust and their sedimentary
786 cover, all of which undergo seafloor hydrothermal alteration prior to subduction. In the ultramafic parts,
787 this alteration is manifest in the oxidation of primary Fe²⁺-bearing phases, such as olivine, pyroxenes,
788 to form Fe³⁺-bearing phases, namely magnetite at high temperature or Fe³⁺-bearing serpentine at low
789 temperatures (Andreani et al. 2013; Klein et al. 2014; Bonnemains et al. 2016). All abyssal peridotites
790 are variably- to highly serpentinised (Mével 2003) and therefore display high Fe³⁺/ΣFe (0.58 ± 0.03 ‰,
791 2SE, *n* = 111; Andreani et al., 2013, 2014; Paulick et al., 2006). However, their iron contents and
792 isotopic compositions are relatively constant, with the exception of peridotites affected by hydrothermal
793 activity (*e.g.*, the Rainbow hydrothermal site) where Fe mobility and therefore isotopic fractionation
794 can be enhanced by the circulation of sulfur-bearing fluids (*e.g.*, Severmann et al., 2004; Debret et al.,
795 2018a). They range from -0.18 ± 0.03 ‰ to 0.10 ± 0.06 ‰ (Craddock et al., 2013 – unweathered
796 samples; Debret et al., 2016; Debret et al., 2018a – non-mineralised samples) with a mean value, -0.03
797 ± 0.03 ‰ (2SE, *n* = 32), indistinguishable from that of orogenic lherzolites (section 5.1.). Although
798 some variations have been observed among different sites; for example the South West Indian (0.00 ±
799 0.03 ‰) and Gakkal ridge (0.01 ± 0.02 ‰) samples display higher δ⁵⁷Fe values relative to Mid-Atlantic
800 Ridge Kane (-0.13 ± 0.02 ‰) and Rainbow (-0.05 ± 0.05 ‰) samples. This difference has been
801 attributed to melting processes occurring prior to oceanic lithosphere alteration (Debret et al., 2018a).
802 Despite large equilibrium isotope fractionation between Fe³⁺ and Fe²⁺ aqueous species and minerals
803 (see section 4.3), these observations suggest that the conversion of peridotites to serpentinites occurs
804 without significant loss or gain of Fe, producing little net change in their Fe isotope compositions.

805 Relative to fresh oceanic basalts, seafloor-altered basalts record larger variations of δ⁵⁷Fe (-2.49 ‰ ≤
806 δ⁵⁷Fe ≤ +2.05 ‰; Rouxel et al., 2003), attributed to crystallisation of secondary Fe-bearing minerals at
807 low temperature (Rouxel et al., 2003). Indeed, the interaction of mafic rocks with seawater results in
808 oxidation from Fe²⁺ to Fe³⁺ through seawater sulfate reduction at high temperature (200–350°C; Shanks
809 et al., 1981) and hydrolysis at low temperature (< 150°C; Bach and Edwards, 2003). The limiting factor
810 for the progress of these reactions is the amount of available reacting seawater (water–rock ratio). Their
811 Fe³⁺/ΣFe is therefore expected to be highest in the uppermost mafic crust (from seafloor to depth of
812 about 200m) where permeability is highest. However, the relatively low mean Fe³⁺/ΣFe (0.22 ± 0.08)
813 of hydrothermally-altered mafic rocks suggests they largely escape oxidation (Lécuyer and Ricard

814 1999). Similarly, highly fractionated $\delta^{57}\text{Fe}$ values in mafic rocks may therefore be restricted to the
815 uppermost crust. Indeed, oceanic mafic rocks show a limited range of Fe isotope compositions; in
816 ophiolite sections ($+0.18 \pm 0.08 \leq \delta^{57}\text{Fe} (\text{‰}) \leq +0.43 \pm 0.11$; Inglis et al., 2017) or at mid-oceanic ridges
817 ($-0.07 \leq \delta^{57}\text{Fe} (\text{‰}) \leq 0.33$; Beard et al., 2003, Nebel et al., 2013, Teng et al., 2013, Weyer and Ionov,
818 2007, Williams et al., 2009). Thus, there is no clear evidence of any significant or consistent leaching
819 or addition of iron in metabasites during hydrothermal alteration at depth.

820 5.2.2. Subducted oceanic lithosphere

821 The subduction of oceanic lithosphere and overlying sediments initiates a continuum of metamorphic
822 reactions and dehydration/rehydration events between the downgoing slab (Schmidt and Poli, 1998),
823 the slab-mantle wedge interface and/or the mantle wedge, which are strongly controlled by intensive
824 variables, such as temperature, pressure and oxygen fugacity ($f\text{O}_2$), and the initial composition and
825 mineralogy of the rocks (e.g., Debret & Sverjensky, 2017; Evans et al., 2017). For a given lithology,
826 the metamorphic evolution is therefore not unique and may vary according to the considered setting.
827 We report here some of the main observations on Fe mobility and redox state in metamorphic lithologies
828 composing meta-ophiolites.

829 Metamorphic ultramafic rocks outcropping in mountain ranges are often highly deformed and
830 recrystallised into antigorite (high P-T variety of serpentine) and metamorphic olivine during prograde
831 metamorphism (e.g., Trommsdorff et al. 1998; Hermann et al. 2000; Padron-Navarta et al. 2011;
832 Scambelluri et al. 2014; Kempf and Hermann 2018). The recrystallisation of slab serpentinites during
833 subduction results in a net decrease of magnetite mode and $\text{Fe}^{3+}/\Sigma\text{Fe}$ (Debret et al., 2014, 2015;
834 Merkulova et al., 2017). In addition, observations of hematite-magnetite assemblages in dehydrated
835 serpentinites (Debret et al., 2015) suggest high $f\text{O}_2$ ($\Delta\text{FMQ}+1$ to $+5$), during antigorite breakdown in
836 subduction zones, compatible with the release of oxidised S and C in slab-derived fluids (Debret &
837 Sverjensky, 2017). Fluid loss is manifest as an increase in subducted serpentinite $\delta^{57}\text{Fe}$ values, which
838 range from $0.00 \pm 0.10 \text{‰}$ to $0.21 \pm 0.10 \text{‰}$ (Debret et al., 2016). The negative correlation between
839 $\delta^{57}\text{Fe}$ and $\text{Fe}^{3+}/\Sigma\text{Fe}$ of bulk serpentinites provides direct evidence for the release of Fe-bearing fluids
840 during serpentinite devolatilisation in subduction zones (Fig. 12; Debret et al., 2016). Such a correlation
841 is consistent with the release of sulfate-rich and/or hypersaline fluids, which preferentially complex
842 isotopically light Fe in the form of $\text{Fe}^{2+}\text{-SO}_x$ or $\text{Fe}^{2+}\text{-Cl}_2$ species, during ultramafic rock devolatilisation.
843 No such correlation is observed in eclogitic rocks from meta-ophiolites, suggesting limited Fe mobility
844 during their dehydration, and their compositions likely reflect protolith variations instead (El Korh et
845 al. 2017; Inglis et al. 2017). In accord with these observations, Huang et al. (2019) report typical basaltic
846 values for eclogites from the Dabie Sulu orogeny, with $-0.01 \pm 0.10 \text{‰}$ to $+0.15 \pm 0.04 \text{‰}$ ($n = 9$),
847 however, they are associated with oxidised, omphacite-epidote veins inferred to have been formed from
848 the breakdown of lawsonite (\pm phengite). These veins have elevated $\text{Fe}^{3+}/\Sigma\text{Fe}$ ($\approx 0.6 - 0.9$) with respect

849 to the adjacent eclogite ($\approx 0.3 - 0.5$) and, consequently higher $\delta^{57}\text{Fe}$, from 0.09 ± 0.06 ‰ to 0.32 ± 0.05
850 ‰ (Huang et al. 2019). Though these veins are concluded to have been locally-derived from the
851 proximal eclogites on the strength of their similar Sr- and Nd-isotope compositions, they could only
852 have constituted a volumetrically minor fraction of the eclogite source rocks in order to leave their iron
853 isotope compositions unperturbed.

854 Analyses of metasedimentary rocks in meta-ophiolites are rather sporadic in the literature and show a
855 limited range of $\delta^{57}\text{Fe}$, from 0.08 ± 0.03 ‰ to 0.17 ± 0.02 ‰ (Inglis et al., 2017). Nebel et al. (2015)
856 analysed a series of currently subducting sediments sampled from the Banda arc whose $\delta^{57}\text{Fe}$ is between
857 $+0.10 \pm 0.07$ to $+0.25 \pm 0.02$ ‰ with a mean of 0.17 ± 0.03 ‰ (2SE, $n = 9$), without any co-variation
858 between $\delta^{57}\text{Fe}$ and detrital element proxies or radiogenic isotope compositions or total organic carbon
859 contents. Siderite (FeCO_3) and ankerite ($\text{Ca}(\text{Fe},\text{Mg},\text{Mn})(\text{CO}_3)_2$) are the most common Fe-bearing
860 carbonates occurring in seafloor sediments. Both phases are expected to preferentially incorporate light
861 iron relative to olivine (Polyakov & Mineev, 2000) and can display highly fractionated $\delta^{57}\text{Fe}$ values
862 down to -2.94 ± 0.03 ‰ in sediments (*e.g.*, Johnson et al. 2008). These minerals are also particularly
863 soluble in fluids emanating at temperatures ranging from 200 to 300 °C during shallow subduction
864 (Milesi et al. 2015) and their dissolution would contribute to the formation of carbonate-bearing fluids
865 with a light Fe isotope signature. Consequently, investigations of carbonated serpentinites from
866 blueschist terrains show that the transfer of carbon-bearing fluids from metasediments to serpentinite
867 can contribute to a strong decrease of $\delta^{57}\text{Fe}$ of serpentinite, down to -0.40 ‰ (Debret et al., 2018b).
868 Although the exact nature of Fe complexation in sediment-derived fluids is poorly constrained, this
869 observation further corroborates the release of isotopically light fluids during sediment decarbonation
870 and dehydration in subduction zones.

871 5.2.3. Iron bearing fluids transferred to the mantle wedge

872 Most studies of meta-ophiolites suggest release of isotopically light Fe in slab-derived fluids during
873 subduction, consistent with the transport of iron with chlorine, sulfate and/or carbonate, as these ligands
874 preferentially complex light Fe with respect to Fe^{3+} -rich antigorite and magnetite (*e.g.*, see section 4.3.,
875 Fujii et al., 2014; Hill et al., 2010). Although the vector of fractionation is correct, it remains unknown
876 whether or not enough Fe can be mobilised in slab-derived fluids to significantly modify the $\delta^{57}\text{Fe}$ of
877 mantle wedge peridotites to produce the light iron isotope composition of arc magmas (Foden et al.
878 2018).

879 Polyphase inclusions trapped in high pressure minerals represent the fluid released at high pressure and
880 temperature during the devolatilisation of the subducting lithosphere in subduction zones. Scambelluri
881 et al. (2015) showed that these olivine-hosted HP-fluids have variable FeO contents from 0.17 to 2.13
882 wt% (assuming $\sum\text{Fe}$ as FeO), in which Cl is often associated with Fe, as inferred from solubility
883 measurements and thermodynamic calculations (see section 4.3.). In addition, the presence of sulfide

884 phases that are not stable in pristine or altered mantle rocks indicates the mobilisation of sulfur
885 concomitant with chlorine and iron. These authors also report the existence of magnesite in inclusions
886 from chlorite harzburgite, providing compelling evidence of carbon mobilisation in the meta-peridotite
887 dehydration fluid.

888 The interaction of slab-derived fluids during their migration through the slab/mantle interface and the
889 mantle wedge may modify their isotopic signature. In order to test how faithfully this fluid signature is
890 transferred to the mantle wedge (*i.e.*, during subduction), Debret et al. (2018b) analysed metamorphic
891 gem olivines in veins from the Sapat complex, part of the sub-arc mantle of the Kohistan-Ladakh Arc.
892 The vein-forming minerals crystallised from a fluid that migrated through the fore-arc mantle, and
893 display light $\delta^{57}\text{Fe}$ values ($-0.13 \pm 0.13 \text{ ‰}$ to $-0.54 \pm 0.14 \text{ ‰}$) relative to that of mantle olivine (*e.g.*,
894 San Carlos olivine $\delta^{57}\text{Fe}$ has $\approx +0.02 \pm 0.05 \text{ ‰}$; Sossi et al., 2015) supporting the hypothesis that they
895 crystallised through reaction with an isotopically fractionated fluid. Similarly, Turner et al. (2018)
896 reported sub-arc mantle xenoliths with light $\delta^{57}\text{Fe}$ (from $+0.03$ to -0.46 ‰) relative to mantle peridotites.
897 Such values are too fractionated to result solely from partial melting and require slab fluid addition
898 and/or diffusive effects that produce light values. This is confirmed by the correlation between $\delta^{57}\text{Fe}$
899 and U/Th ratios in these sub-arc xenoliths. Although not all sub-arc peridotites show such isotopically
900 light values (section 5.1.1.), these observations provide empirical evidence for the transfer of
901 isotopically light Fe across subduction zones, in which Fe can be complexed by chlorine or sulfate or
902 carbonate anions. Existing models (Huang et al. 2019) suggest, given the composition of polyphase
903 inclusions (Scambelluri et al. 2015) and inferred iron isotope fractionation factors between olivine and
904 fluids (Debret et al. 2018), that 30 – 40 % fluid addition to the mantle wedge would be required to shift
905 their iron isotope compositions to sufficiently light values observed in some arc basalts (-0.15 ‰ ; Foden
906 et al. 2018), but this increases to unrealistically high values for sub-arc mantle xenoliths with
907 compositions as low as -0.46 ‰ (Turner et al. 2018). The predominant uncertainties with such models
908 remain (*i*) the fraction of fluid permitted to metasomatise the mantle wedge, (*ii*) its iron content and iron
909 isotope composition (*iii*) the degree of disequilibrium during fluid-rock interaction and (*iv*) the nature
910 and identity of the Fe-bearing fluid species. Determining the dominant Fe-bearing species will require
911 experimental work that can produce thermodynamic data for these species at the pressures, temperatures
912 and compositions of interest.

913 **6.0. Conclusion**

914 At the high temperature conditions relevant to the formation of igneous and metamorphic rocks, the
915 differences in the ground-state vibrational frequencies of isotopic substitutions, a quantum mechanical
916 phenomenon, control isotope partitioning between two phases. These frequencies are in turn determined
917 by the bonding environment of iron; where higher redox state and lower co-ordination number tends to
918 favour the heavier isotopes. Similarly, a reduction in partial molar volume of the iron-bearing site in a
919 condensed phase due to either increasing pressure and/or a transition to a low spin electronic

920 configuration engenders bond contraction and strengthening, also concentrating the heavier isotopes.
921 The role of changing redox state and co-ordination environment in modifying iron force constants is
922 highlighted, particularly along mineral solid solutions, magmatic liquid compositional series (basalt to
923 rhyolite) and for different ligand identities and complexation stoichiometries in aqueous fluids.

924 Partial melting in the Earth's upper mantle results in small ($\approx +0.05\%$) iron isotopic enrichment in the
925 liquid relative to its source because isotopically-heavy, ferric iron is preferentially concentrated in the
926 melt with respect to lighter ferrous iron, in addition to its slightly lower mean co-ordination number in
927 silicate liquids relative to minerals. The difference between the melt and its residue decreases with
928 higher degrees of melting and in more reduced sources. Contrastingly, the degree of iron isotopic
929 enrichment in the melt is enhanced in some ocean island basalts due to the presence of heavy isotope-
930 enriched mafic, garnet-bearing components with respect to mid-ocean ridge basalts. Arc magmas are,
931 on average, lighter still, and have iron isotope compositions that are inversely correlative with the *i*) age
932 of the subducting slab and *ii*) its downgoing velocity. The mechanisms that contribute to this isotopic
933 signature may include continued episodes of light, fluid-fluxed melting in stationary sub-arc mantle that
934 are continuously depleted with time in mature subduction zones. However, understanding the relative
935 contribution of each process requires concerted experimental, natural and spectroscopic work to
936 determine the budget, speciation and transport of iron in subduction zones.

937 Magmatic rocks show a tendency towards heavy isotope-enriched compositions with increasing
938 differentiation; however, the conditions under which these liquids cool and crystallise controls their
939 subsequent evolution. Isotopic equilibria between minerals and melt play a predominant role in
940 determining their liquid line of descent; conditions closed to O_2 exchange result in heavy isotope
941 enrichment in mafic tholeiitic systems, whereas systems open O_2 exchange (typically calc-alkaline
942 magmas in arc environments) exhibit little change in their iron isotope composition prior to $\approx 65\text{-}70\%$
943 SiO_2 . The uniformly heavy iron isotope composition of granites above this value stems from a
944 strengthening of Fe-O bonds in alkali-rich siliceous melts in tandem with crystallisation of Fe^{2+} -bearing
945 phases. Because A-type granites undergo more extensive crystal fractionation than do S- and
946 particularly I-types, they tend to have the heaviest isotopic compositions, while the Fe^{3+} -rich mineral
947 assemblage of I-type granites limits heavy isotopic enrichment.

948 Metamorphism accompanying cooling of the oceanic lithosphere and its hydration at mid-oceanic
949 ridges imparts surprisingly little- to no iron isotopic fractionation at the lithospheric scale, whereas local
950 reactions in the uppermost mafic crust or nearby hydrothermal areas (*e.g.*, Rainbow hydrothermal site)
951 show evidence for iron mobility relative to fresh basalts or peridotites. The analyses of mafic rocks in
952 high pressure meta-ophiolites appear to record primary magmatic signatures and have imprints inherited
953 from prior partial melting episodes. In contrast, sedimentary and ultramafic rocks show progressively
954 heavier iron isotope compositions with increasing metamorphic grade, consistent with the loss of Fe^{2+} -
955 bearing species with an isotopically light signature, in which iron is likely complexed by chlorides or
956 oxidised ligands (*i.e.*, sulfate or carbonate). Whether iron is sufficiently concentrated in these fluids to
957 influence the iron isotope composition of the sub-arc mantle remains an area of research.

958 **Acknowledgements**

959 PAS was supported by the European Research Council under the H2020 framework program/ERC grant
960 agreement #637503 (PRISTINE) at IPGP and by an SNF Ambizione Fellowship (#180025) at ETH
961 Zürich. We thank Marc Blanchard and an anonymous reviewer for their thoughtful and constructive
962 reviews.

For Review Only

963 **References**

- 964 Andreani M, Escartin J, Delacour A, et al (2014) Tectonic structure, lithology, and hydrothermal
965 signature of the rainbow massif (Mid-Atlantic Ridge 36° 14'N). *Geochemistry, Geophys*
966 *Geosystems* 15:3543–3571. doi: 10.1002/2014GC005269
- 967 Andreani M, Muñoz M, Marcaillou C, Delacour A (2013) μ XANES study of iron redox state in
968 serpentine during oceanic serpentinization. *Lithos* 178:70–83. doi: 10.1016/j.lithos.2013.04.008
- 969 Arató R, Audétat A (2019) Magnetite – silicate melt oxybarometry. (This volume).
- 970 Armstrong K, Frost DJ, McCammon CA, et al (2017) The Effect of Pressure on Iron Speciation in
971 Silicate Melts at a Fixed Oxygen Fugacity: The Possibility of a Redox Profile Through a
972 Terrestrial Magma Ocean. AGU Fall Meeting, #MR54A-04
- 973 Asimow PD, Hirschmann MM, Stolper EM (1997) An analysis of variations in isentropic melt
974 productivity. *Philos Trans R Soc A Math Phys Eng Sci* 355:255–281. doi:
975 10.1098/rsta.1997.0009
- 976 Ayers JC, Dittmer SK, Layne GD (1997) Partitioning of elements between peridotite and H₂O at 2.0–
977 3.0 GPa and 900–1100 °C, and application to models of subduction zone processes. *Earth Planet*
978 *Sci Lett* 150:381–398. doi: 10.2134/jeq2005.0109
- 979 Bach W, Edwards KJ (2003) Iron and sulfide oxidation within the basaltic ocean crust: Implications
980 for chemolithoautotrophic microbial biomass production. *Geochim Cosmochim Acta* 67:3871–
981 3887. doi: 10.1016/S0016-7037(03)00304-1
- 982 Badro J, Fiquet G, Guyot F, et al (2003) Iron partitioning in Earth's mantle: toward a deep lower
983 mantle discontinuity. *Science* 300:789–791. doi: 10.1126/science.1081311
- 984 Badro J, Rueff J-P, Vankó G, et al (2004) Electronic Transitions in Perovskite: Possible
985 Nonconvecting Layers in the Lower Mantle. *Science* 305:383–386. doi:
986 10.1126/science.1098840
- 987 Baldridge WS, McGetchin TR, Frey FA, Jarosewich E (1973) Magmatic evolution of Hekla, Iceland.
988 *Contrib to Mineral Petrol* 42:245–258. doi: 10.1007/BF00371589
- 989 Barnes SJ, Roeder PL (2001) The Range of Spinel Compositions in Terrestrial Mafic and Ultramafic
990 Rocks. *J Petrol* 42:2279–2302.
- 991 Beard BL, Johnson CM, Skulan JL, et al (2003a) Application of Fe isotopes to tracing the
992 geochemical and biological cycling of Fe. *Chem Geol* 195:87–117. doi: 10.1016/S0009-
993 2541(02)00390-X
- 994 Beard BL, Johnson CM, Von Damm KL, Poulson RL (2003b) Iron isotope constraints on Fe cycling
995 and mass balance in oxygenated Earth oceans. *Geology* 31:629–632. doi: 10.1130/0091-
996 7613(2003)031<0629:IICOFC>2.0.CO;2
- 997 Bénard A, Woodland AB, Arculus RJ, et al (2018) Variation in sub-arc mantle oxygen fugacity
998 during partial melting recorded in refractory peridotite xenoliths from the West Bismarck Arc.
999 *Chem Geol* 486:16–30. doi: 10.1016/j.chemgeo.2018.03.004
- 1000 Berry AJ, Yaxley GM, Woodland AB, Foran GJ (2010) A XANES calibration for determining the
1001 oxidation state of iron in mantle garnet. *Chem Geol* 278:31–37. doi:
1002 10.1016/j.chemgeo.2010.08.019
- 1003 Berry AJ, Stewart GA, O'Neill HSC, et al (2018) A re-assessment of the oxidation state of iron in
1004 MORB glasses. *Earth Planet Sci Lett* 483:114–123. doi: 10.1016/j.epsl.2017.11.032
- 1005 Bigeleisen J, Mayer MG (1947) Calculation of Equilibrium Constants for Isotopic Exchange
1006 Reactions. *J Chem Phys* 15:261–267. doi: 10.1063/1.1746492

- 1007 Bilenker LD, VanTongeren JA, Lundstrom CC, Simon AC (2017) Iron isotopic evolution during
1008 fractional crystallization of the uppermost Bushveld Complex layered mafic intrusion.
1009 Geochemistry, Geophys Geosystems 18:2016GC006660. doi:
1010 10.1002/2016GC006679.Received
- 1011 Blanchard M, Poitrasson F, Méheut M, et al (2009) Iron isotope fractionation between pyrite (FeS₂),
1012 hematite (Fe₂O₃) and siderite (FeCO₃): A first-principles density functional theory study.
1013 Geochim Cosmochim Acta 73:6565–6578. doi: 10.1016/j.gca.2009.07.034
- 1014 Blanchard M, Dauphas N (2019) Oxidation state, coordination, and covalency controls on iron
1015 isotopic fractionation in Earth’s mantle and crust: Insights from first-principles calculations and
1016 NRIXS spectroscopy. (this volume)
- 1017 Boctor NZ, Popp RK, Frantz JD (1980) Mineral-solution equilibria-IV. Solubilities and the
1018 thermodynamic properties of FeCl₂ in the system Fe₂O₃-H₂-H₂O-HCl. Geochim Cosmochim
1019 Acta 44:1509–1518.
- 1020 Bonnemains D, Carlut J, Escartín J, et al (2016) Magnetic signatures of serpentinization at ophiolite
1021 complexes. Geochemistry, Geophys Geosystems 17:2969–2986. doi: 10.1002/2016GC006321
- 1022 Borisov A, Behrens H, Holtz F (2017) Effects of strong network modifiers on Fe³⁺/Fe²⁺ in silicate
1023 melts: an experimental study. Contrib to Mineral Petrol 172:34. doi: 10.1007/s00410-017-1337-
1024 1
- 1025 Borisov A, McCammon C (2010) The effect of silica on ferric/ferrous ratio in silicate melts: An
1026 experimental study using Mössbauer spectroscopy. Am Mineral 95:545–555. doi:
1027 10.2138/am.2010.3217
- 1028 Bosi F, Halenius U, Skogby H (2009) Crystal chemistry of the magnetite-ulvospinel series. Am
1029 Mineral 94:181–189. doi: 10.2138/am.2009.3002
- 1030 Bourdon B, Roskosz M, Hin RC (2018) Isotope tracers of core formation. Earth-Science Rev 181:61–
1031 81. doi: 10.1016/J.EARSCIREV.2018.04.006
- 1032 Brugger J, Liu W, Etschmann B, et al (2016) A review of the coordination chemistry of hydrothermal
1033 systems, or do coordination changes make ore deposits? Chem Geol 447:219–253. doi:
1034 10.1016/j.chemgeo.2016.10.021
- 1035 Buddington AF, Lindsley DH (1964) Iron-Titanium Oxide Minerals and Synthetic Equivalents. J
1036 Petrol 5:310–357. doi: 10.1093/petrology/5.2.310
- 1037 Burnham CW (1979) Magmas and hydrothermal fluids. In: Barnes HL (ed) Geochemistry of
1038 Hydrothermal Ore Deposits, 2nd edn. John Wiley & Sons, New York, pp 71–136
- 1039 Cameron M, Sueno S, Prewitt CT, Papike JJ (1973) High-Temperature Crystal Chemistry of Acmite ,
1040 Diopside, Hedenbergite, Jadeite, Spodumene and Ureyite. Am Mineral 58:594–618.
- 1041 Candela PA (1989) Magmatic ore-forming fluids: thermodynamic and mass transfer calculations of
1042 metal concentrations. In: Whitney JA, J NA (eds) Ore Deposition Associated with Magmas :
1043 Soc.Econ.Geol., Reviews in Economic Geology. pp 203–221
- 1044 Canil D, O’Neill HSC (1996) Distribution of Ferric Iron in some Upper-Mantle Assemblages. J Petrol
1045 37:609–635.
- 1046 Canil D, O’Neill HSC, Pearson DG, et al (1994) Ferric iron in peridotites and mantle oxidation states.
1047 Earth Planet Sci Lett 123:205–220. doi: 10.1016/0012-821X(94)90268-2
- 1048 Carmichael ISE (1967) The mineralogy of Thingmuli, a Tertiary’ volcano in eastern Iceland. Am J
1049 Sci 276:309–329.
- 1050 Carmichael ISE (1991) The redox states of basic and silicic magmas: a reflection of their source

- 1051 regions? *Contrib to Mineral Petrol* 106:129–141. doi: 10.1007/BF00306429
- 1052 Chappell BW, White AJR (1974) Two contrasting granite types. *Pacific Geol* 8:173–174.
- 1053 Chen L-M, Song X-Y, Zhu X-K, et al (2014) Iron isotope fractionation during crystallization and sub-
1054 solidus re-equilibration: Constraints from the Baima mafic layered intrusion, SW China. *Chem*
1055 *Geol* 380:97-109. doi: 10.1016/j.chemgeo.2014.04.020
- 1056 Chou I-M, Eugster HP (1977) Solubility of Magnetite in Supercritical Chloride Solutions. *Am J Sci*
1057 277:1296–1314.
- 1058 Craddock PR, Warren JM, Dauphas N (2013) Abyssal peridotites reveal the near-chondritic Fe
1059 isotopic composition of the Earth. *Earth Planet Sci Lett* 365:63–76.
- 1060 Dauphas N, Craddock PR, Asimow PD, et al (2009) Iron isotopes may reveal the redox conditions of
1061 mantle melting from Archean to Present. *Earth Planet Sci Lett* 288:255–267.
- 1062 Dauphas N, Roskosz M, Alp EE, et al (2012) A general moment NRIXS approach to the
1063 determination of equilibrium Fe isotopic fractionation factors: Application to goethite and
1064 jarosite. *Geochim Cosmochim Acta* 94:254–275. doi: 10.1016/j.gca.2012.06.013
- 1065 Dauphas N, Roskosz M, Alp EE, et al (2014) Magma redox and structural controls on iron isotope
1066 variations in Earth's mantle and crust. *Earth Planet Sci Lett* 398:127–140. doi:
1067 10.1016/j.epsl.2014.04.033
- 1068 Davies DR, Le Voci G, Goes S, et al (2016) The mantle wedge's transient 3-D flow regime and
1069 thermal structure. *Geochemistry, Geophys Geosystems* 17:78–100.
- 1070 Davis FA, Humayun M, Hirschmann MM, Cooper RS (2013) Experimentally determined
1071 mineral/melt partitioning of first-row transition elements (FRTE) during partial melting of
1072 peridotite at 3GPa. *Geochim Cosmochim Acta* 104:232–260. doi: 10.1016/j.gca.2012.11.009
- 1073 Debret B, Andreani M, Muñoz M, et al (2014) Evolution of Fe redox state in serpentinite during
1074 subduction. *Earth Planet Sci Lett* 400:206–218. doi: 10.1016/j.epsl.2014.05.038
- 1075 Debret B, Beunon H, Mattielli N, Andreani M, Ribeiro Da Costa I, Escartin J (2018a). Ore component
1076 mobility, transport and mineralization at mid-oceanic ridges: a stable isotopes (Zn, Cu and Fe)
1077 study of the Rainbow massif (Mid-Atlantic Ridge 36°14'N). *Earth Planet Sci Lett* 503:170-180,
1078 doi:10.1016/j.epsl.2018.09.009
- 1079 Debret B, Bolfan-Casanova N, Padrón-Navarta JA, et al (2015) Redox state of iron during high-
1080 pressure serpentinite dehydration. *Contrib to Mineral Petrol* 169:1–18. doi: 10.1007/s00410-015-
1081 1130-y
- 1082 Debret B, Bouilhol P, Pons ML, Williams H (2018b) Carbonate Transfer during the Onset of Slab
1083 Devolatilization: New Insights from Fe and Zn Stable Isotopes. *J Petrol* 59:1145–1166. doi:
1084 10.1093/petrology/egy057
- 1085 Debret B, Millet MA, Pons ML, Bouilhol P, Inglis E, Williams H (2016). Isotopic evidence for iron
1086 mobility during subduction. *Geology* 44:215-218.
- 1087 Debret B, Sverjensky DA (2017) Highly oxidising fluids generated during serpentinite breakdown in
1088 subduction zones. *Sci Rep* 7:1–6. doi: 10.1038/s41598-017-09626-y
- 1089 Dickenson MP, Hess PC (1986) The structural role and homogeneous redox equilibria of iron in
1090 peraluminous, metaluminous and peralkaline silicate melts. *Contrib to Mineral Petrol* 92:207–
1091 217.
- 1092 Ding K, Seyfried WE (1992) Determination of Fe-Cl complexing in the low pressure supercritical
1093 region (NaCl fluid): Iron solubility constraints on pH of subseafloor hydrothermal fluids.
1094 *Geochim Cosmochim Acta* 56:3681–3692. doi: 10.1016/0016-7037(92)90161-B

- 1095 Du DH, Wang XL, Yang T, et al (2017) Origin of heavy Fe isotope compositions in high-silica
1096 igneous rocks: A rhyolite perspective. *Geochim Cosmochim Acta* 218:58–72. doi:
1097 10.1016/j.gca.2017.09.014
- 1098 Evans KA, Reddy SM, Tomkins AG, et al (2017) Effects of geodynamic setting on the redox state of
1099 fluids released by subducted mantle lithosphere. *Lithos* 278-281:26–42. doi:
1100 10.1016/j.lithos.2016.12.023
- 1101 Evans K-A, Tomkins A-G (2011) The relationship between subduction zone redox budget and arc
1102 magma fertility. *Earth Planet Sci Lett* 308:401–409. doi: 10.1016/j.epsl.2011.06.009
- 1103 Farges F, Lefrère Y, Rossano S, et al (2004) The effect of redox state on the local structural
1104 environment of iron in silicate glasses: a combined XAFS spectroscopy, molecular dynamics,
1105 and bond valence study. *J Non Cryst Solids* 344:176–188. doi: 10.1016/j.jnoncrystol.2004.07.050
- 1106 Fein JB, Hemley JJ, Angelo WMD, et al (1992) Experimental study of iron-chloride complexing in
1107 hydrothermal fluids. *Geochim Cosmochim Acta* 56:3179–3190. doi: 10.1016/0016-
1108 7037(92)90296-U
- 1109 Foden J, Sossi PA, Nebel O (2018) Controls on the iron isotopic composition of global arc magmas.
1110 *Earth Planet Sci Lett*. doi: 10.1016/j.epsl.2018.04.039
- 1111 Foden J, Sossi PA, Wawryk CM (2015) Fe isotopes and the contrasting petrogenesis of A-, I- and S-
1112 type granite. *Lithos* 212-215:32–44. doi: 10.1016/j.lithos.2014.10.015
- 1113 Frost CD, Frost BR (2010) On Ferroan (A-type) Granitoids: their Compositional Variability and
1114 Modes of Origin. *J Petrol* 52:39–53. doi: 10.1093/petrology/egq070
- 1115 Fujii T, Moynier F, Blichert-Toft J, Albarède F (2014) Density functional theory estimation of isotope
1116 fractionation of Fe, Ni, Cu, and Zn among species relevant to geochemical and biological
1117 environments. *Geochim Cosmochim Acta* 140:553–576. doi: 10.1016/j.gca.2014.05.051
- 1118 Fujino K, Nishio-Hamane D, Seto Y, et al (2012) Spin transition of ferric iron in Al-bearing Mg-
1119 perovskite up to 200 GPa and its implication for the lower mantle. *Earth Planet Sci Lett* 317-
1120 318:407–412. doi: 10.1016/J.EPSL.2011.12.006
- 1121 Hawthorne FC (1978) The Crystal Chemistry of the Amphiboles. VIII. The Crystal Structure and Site
1122 Chemistry of Fluor-Riebeckite. *Can Mineral* 16:187–194.
- 1123 He Y, Wu H, Ke S, et al (2017) Iron isotopic compositions of adakitic and non-adakitic granitic
1124 magmas: Magma compositional control and subtle residual garnet effect. *Geochim Cosmochim*
1125 *Acta* 203:89–102. doi: 10.1016/j.gca.2017.01.005
- 1126 Heimann A, Beard BL, Johnson CM (2008) The role of volatile exsolution and sub-solidus fluid/rock
1127 interactions in producing high $^{56}\text{Fe}/^{54}\text{Fe}$ ratios in siliceous igneous rocks. *Geochim Cosmochim*
1128 *Acta* 72:4379–4396. doi: 10.1016/j.gca.2008.06.009
- 1129 Hermann J, Müntener O, Scambelluri M (2000) The importance of serpentinite mylonites for
1130 subduction and exhumation of oceanic crust. *Tectonophysics* 327:225–238. doi: 10.1016/S0040-
1131 1951(00)00171-2
- 1132 Hill PS, Schauble E a., Shahar A, et al (2009) Experimental studies of equilibrium iron isotope
1133 fractionation in ferric aquo-chloro complexes. *Geochim Cosmochim Acta* 73:2366–2381. doi:
1134 10.1016/j.gca.2009.01.016
- 1135 Hill PS, Schauble E a., Young ED (2010) Effects of changing solution chemistry on $\text{Fe}^{3+}/\text{Fe}^{2+}$ isotope
1136 fractionation in aqueous Fe–Cl solutions. *Geochim Cosmochim Acta* 74:6669–6689. doi:
1137 10.1016/j.gca.2010.08.038
- 1138 Hill PS, Schauble EA (2008) Modeling the effects of bond environment on equilibrium iron isotope
1139 fractionation in ferric aquo-chloro complexes. *Geochim Cosmochim Acta* 72:1939–1958.

- 1140 Hirschmann MM, Ghiorso MS, Stolper M (1999) Calculation of Peridotite Partial Melting from
1141 Thermodynamic Models of Minerals and Melts. II. Isobaric Variations in Melts near the Solidus
1142 and owing to Variable Source Composition. *J Petrol* 40:297–313. doi: 10.1093/петroj/40.2.297
- 1143 Huang F, Zhang Z, Lundstrom CC, Zhi X (2011) Iron and magnesium isotopic compositions of
1144 peridotite xenoliths from Eastern China. *Geochim Cosmochim Acta* 75:3318–3334. doi:
1145 10.1016/j.gca.2011.03.036
- 1146 Huang J, Guo S, Jin Q-Z, Huang F (2019) Iron and magnesium isotopic compositions of subduction-
1147 zone fluids and implications for arc volcanism. *Geochim Cosmochim Acta*. In press.
1148 10.1016/j.gca.2019.06.020
- 1149 Inglis EC, Debret B, Burton KW, et al (2017) The behavior of iron and zinc stable isotopes
1150 accompanying the subduction of mafic oceanic crust: A case study from Western Alpine
1151 ophiolites. *Geochemistry, Geophys Geosystems* 18:2562–2579. doi: 10.1002/2016GC006735
- 1152 Jackson JM, Sturhahn W, Shen G, et al (2005a) A synchrotron Mössbauer spectroscopy study of
1153 (Mg,Fe)SiO₃ perovskite up to 120 GPa. *Am Mineral* 90:199–205. doi: 10.2138/am.2005.1633
- 1154 Jackson WE, Farges F, Yeager M, et al (2005b) Multi-spectroscopic study of Fe(II) in silicate glasses:
1155 Implications for the coordination environment of Fe(II) in silicate melts. *Geochim Cosmochim*
1156 *Acta* 69:4315–4332. doi: 10.1016/j.gca.2005.01.008
- 1157 Jayasuriya KD, O'Neill HSC, Berry AJ, Campbell SJ (2004) A Mössbauer study of the oxidation state
1158 of Fe in silicate melts. *Am Mineral* 89:1597–1609.
- 1159 Johnson CM, Beard BL, Klein C, et al (2008) Iron isotopes constrain biologic and abiologic processes
1160 in banded iron formation genesis. *Geochim Cosmochim Acta* 72:151–169. doi:
1161 10.1016/J.GCA.2007.10.013
- 1162 Kelley KA, Cottrell E (2009) Water and the Oxidation State of Subduction Zone Magmas. *Science*
1163 325:605–607. doi: 10.1126/science.1174156
- 1164 Kempf ED, Hermann J (2018) Hydrogen incorporation and retention in metamorphic olivine during
1165 subduction: Implications for the deep water cycle. *Geology* 46:571–574. doi: 10.1130/G40120.1
- 1166 Kinzler RJ, Grove TL (1992) Primary Magmas of Mid-Ocean Ridge Basalts 1. Experiments and
1167 Methods. *J Geophys Res* 97:6885–6906.
- 1168 Kirby SH, Engdahl RE, Denlinger R (1996) Intermediate-Depth Intraslab Earthquakes and Arc
1169 Volcanism as Physical Expressions of Crustal and Uppermost Mantle Metamorphism in
1170 Subducting Slabs. In: Bebout GE, Scholl DW, Kirby SH, Platt JP (eds) *Subduction: Top to*
1171 *Bottom*. American Geophysical Union, Washington DC, pp 195–214
- 1172 Klein F, Bach W, Humphris SE, et al (2014) Magnetite in seafloor serpentinite-Some like it hot.
1173 *Geology* 42:135–138. doi: 10.1130/G35068.1
- 1174 Knipping JL, Behrens H, Wilke M, et al (2015) Effect of oxygen fugacity on the coordination and
1175 oxidation state of iron in alkali bearing silicate melts. *Chem Geol* 411:143–154. doi:
1176 10.1016/j.chemgeo.2015.07.004
- 1177 Konter JG, Pietruszka AJ, Hanan BB, et al (2016) Unusual $\delta^{56}\text{Fe}$ values in Samoan rejuvenated lavas
1178 generated in the mantle. *Earth Planet Sci Lett* 450:221–232. doi: 10.1016/j.epsl.2016.06.029
- 1179 Kress VC, Carmichael ISE (1991) The compressibility of silicate liquids containing Fe₂O₃ and the
1180 effect of composition, temperature, oxygen fugacity and pressure on their redox states. *Contrib*
1181 *to Mineral Petrol* 108:82–92. doi: 10.1007/BF00307328
- 1182 Kwak TAP, Brown WM, Abeysinghe PB, Teong Hing Tan (1986) Fe solubilities in very saline
1183 hydrothermal fluids: their relation to zoning in some ore deposits. *Econ Geol* 81:447–465. doi:
1184 10.2113/gsecongeo.81.2.447

- 1185 Lange RA, Carmichael ISE (1987) Densities of Na₂O-K₂O-CaO-MgO-FeO-Fe₂O₃-Al₂O₃-TiO₂-SiO₂
1186 liquids: New measurements and derived partial molar properties. *Geochim Cosmochim Acta*
1187 51:2931–2946. doi: 10.1016/0016-7037(87)90368-1
- 1188 Lécuyer C, Ricard Y (1999) Long-term fluxes and budget of ferric iron: Implication for the redox
1189 states of the Earth's mantle and atmosphere. *Earth Planet Sci Lett* 165:197–211. doi:
1190 10.1016/S0012-821X(98)00267-2
- 1191 Lee C-TA, Leeman WP, Canil D, Li Z-XA (2005) Similar V/Sc Systematics in MORB and Arc
1192 Basalts: Implications for the Oxygen Fugacities of their Mantle Source Regions. *J Petrol*
1193 46:2313–2336. doi: 10.1093/petrology/egi056
- 1194 Li C, Ripley EM (2009) Sulfur contents at sulfide-liquid or anhydrite saturation in silicate
1195 melts: Empirical equations and example applications. *Econ Geol* 104:405–412. doi:
1196 10.2113/gsecongeo.104.3.405
- 1197 Li J-X, Qin K-Z, Li G-M, et al (2018) Iron isotope fractionation during magmatic-hydrothermal
1198 evolution: A case study from the Duolong porphyry Cu-Au deposit, Tibet. *Geochim Cosmochim*
1199 *Acta* 238:1–15. doi: 10.1016/J.GCA.2018.07.008
- 1200 Li Q-W, Nebel O, Nebel-Jacobsen Y et al (2019) Crustal reworking at convergent margins traced by
1201 Fe isotopes in I-type intrusions from the Gangdese arc, Tibetan Plateau. *Chem Geol* 510:47–55.
- 1202 Lin J-F, Speziale S, Mao Z, Marquardt H (2013) Effects of the electronic spin transition of iron in
1203 lower mantle minerals: implications for deep mantle geophysics and geochemistry. *Rev*
1204 *Geophys* 51:244–275. doi: 10.1002/rog.20010
- 1205 Linnen RL, Keppler H (2002) Melt composition control of Zr/Hf fractionation in magmatic processes.
1206 *Geochim Cosmochim Acta* 66:3293–3301.
- 1207 Liu J, Dauphas N, Roskosz M, et al (2017) Iron isotopic fractionation between silicate mantle and
1208 metallic core at high pressure. *Nat Commun* 8:14377 doi: 10.1038/ncomms14377
- 1209 Liu P-P, Zhou M-F, Luais B, et al (2014) Disequilibrium iron isotopic fractionation during the high-
1210 temperature magmatic differentiation of the Baima Fe–Ti oxide-bearing mafic intrusion, SW
1211 China. *Earth Planet Sci Lett* 399:21–29. doi: 10.1016/j.epsl.2014.05.002
- 1212 Lundgaard KL, Tegner C (2004) Partitioning of ferric and ferrous iron between plagioclase and
1213 silicate melt. *Contrib to Mineral Petrol* 147:470–483. doi: 10.1007/s00410-004-0568-0
- 1214 Mallmann G, O'Neill HSC (2009) The Crystal/Melt Partitioning of V during Mantle Melting as a
1215 Function of Oxygen Fugacity Compared with some other Elements (Al, P, Ca, Sc, Ti, Cr, Fe,
1216 Ga, Y, Zr and Nb). *J Petrol* 50:1765–1794. doi: 10.1093/petrology/egp053
- 1217 Manning CE (2004) The chemistry of subduction-zone fluids. *Earth Planet Sci Lett* 223:1–16. doi:
1218 10.1016/j.epsl.2004.04.030
- 1219 Mathez EA (1984) Influence of degassing on oxidation states of basaltic magmas. *Nature* 310:371–
1220 375.
- 1221 McCammon C (1997) Perovskite as a possible sink for ferric iron in the lower mantle. *Nature*
1222 387:694–696. doi: 10.1038/42685
- 1223 McCammon C, Dubrovinsky L, Narygina O, et al (2010) Low-spin Fe²⁺ in silicate perovskite and a
1224 possible layer at the base of the lower mantle. *Phys Earth Planet Inter* 180:215–221. doi:
1225 10.1016/J.PEPI.2009.10.012
- 1226 Merkulova M V., Muñoz M, Brunet F, et al (2017) Experimental insight into redox transfer by iron-
1227 and sulfur-bearing serpentinite dehydration in subduction zones. *Earth Planet Sci Lett* 479:133–
1228 143. doi: 10.1016/j.epsl.2017.09.009

- 1229 Mével C (2003) Serpentinization of abyssal peridotites at mid-ocean ridges. *Comptes Rendus Geosci*
1230 335:825–852. doi: 10.1016/j.crte.2003.08.006
- 1231 Milesi V, Guyot F, Brunet F, et al (2015) Formation of CO₂, H₂ and condensed carbon from siderite
1232 dissolution in the 200–300°C range and at 50 MPa. *Geochim Cosmochim Acta* 154:201–211.
1233 doi: 10.1016/j.gca.2015.01.015
- 1234 Nebel O, Arculus RJ, Sossi PA, et al (2013) Iron isotopic evidence for convective resurfacing of
1235 recycled arc-front mantle beneath back-arc basins. *Geophys Res Lett* 40:5849–5853. doi:
1236 10.1002/2013GL057976
- 1237 Nebel O, Sossi PA, Bénard A, et al (2015) Redox-variability and controls in subduction zones from an
1238 iron-isotope perspective. *Earth Planet Sci Lett* 432:142–151. doi: 10.1016/j.epsl.2015.09.036
- 1239 Nebel O, Sossi PA, Foden J et al. (2018) Iron isotope variability in ocean floor lavas and mantle
1240 sources in the Lau back-arc basin. *Geochim Cosmochim Acta* 241:150–163. doi:
1241 10.1016/j.gca.2018.08.046
- 1242 Nell J, Wood BJ, Mason TO (1989) High-temperature cation distributions in Fe₃O₄-MgAl₂O₄-
1243 MgFe₂O₄-FeAl₂O₄ spinels from thermopower and conductivity measurement. *Am Mineral*
1244 74:339–351.
- 1245 O'Neill HSC, Berry AJ, McCammon CC, et al (2006) An experimental determination of the effect of
1246 pressure on the Fe³⁺/ΣFe ratio of an anhydrous silicate melt to 3.0 GPa. *Am Mineral* 91:404–
1247 412. doi: 10.2138/am.2005.1929
- 1248 O'Neill HSC, Mavrogenes JA (2002) The Sulfide Capacity and the Sulfur Content at Sulfide
1249 Saturation of Silicate Melts at 1400 °C and 1 bar. *J Petrol* 43:1049–1087.
- 1250 O'Neill HSC, Navrotsky A (1984) Cation distributions and thermodynamic properties of binary spinel
1251 solid solutions. *Am Mineral* 69:733–753.
- 1252 Padron-Navarta J a., Lopez Sanchez-Vizcaino V, Garrido CJ, Gomez-Pugnaire MT (2011)
1253 Metamorphic Record of High-pressure Dehydration of Antigorite Serpentinite to Chlorite
1254 Harzburgite in a Subduction Setting (Cerro del Almirez, Nevado-Filabride Complex, Southern
1255 Spain). *J Petrol* 52:2047–2078. doi: 10.1093/petrology/egr039
- 1256 Paulick H, Bach W, Godard M, et al (2006) Geochemistry of abyssal peridotites (Mid-Atlantic Ridge,
1257 15°20'N, ODP Leg 209): Implications for fluid/rock interaction in slow spreading environments.
1258 *Chem Geol* 234:179–210. doi: 10.1016/j.chemgeo.2006.04.011
- 1259 Pauling L (1929) The Principles Determining the Structure of Complex Ionic Crystals. *J Am Chem*
1260 *Soc* 51:1010–1026.
- 1261 Peters BJ, Shahar A, Carlson RW, et al (2019) A sulfide perspective on iron isotope fractionation
1262 during ocean island basalt petrogenesis. *Geochim Cosmochim Acta* 245:59–78. doi:
1263 10.1016/J.GCA.2018.10.015
- 1264 Petric A, Jacob KT, Alcock CB (1981) Thermodynamic Properties of Fe₃O₄-FeAl₂O₄ Spinel Solid
1265 Solutions. *J Am Ceram Soc* 64:632–639. doi: 10.1111/j.1151-2916.1981.tb15860.x
- 1266 Poitrasson F, Delpech G, Grégoire M (2013) On the iron isotope heterogeneity of lithospheric mantle
1267 xenoliths: implications for mantle metasomatism, the origin of basalts and the iron isotope
1268 composition of the Earth. *Contrib to Mineral Petrol* 165:1243–1258. doi: 10.1007/s00410-013-
1269 0856-7
- 1270 Poitrasson F, Freyrier R (2005) Heavy iron isotope composition of granites determined by high
1271 resolution MC-ICP-MS. *Chem Geol* 222:132–147. doi: 10.1016/j.chemgeo.2005.07.005
- 1272 Poitrasson F, Halliday AN, Lee D-C, et al (2004) Iron isotope differences between Earth, Moon, Mars
1273 and Vesta as possible records of contrasted accretion mechanisms. *Earth Planet Sci Lett*

- 1274 223:253–266.
- 1275 Poli S, Schmidt MW (2002) Petrology of Subducted Slabs. *Annu Rev Earth Planet Sci* 30:207–235.
1276 doi: 10.1146/annurev.earth.30.091201.140550
- 1277 Polyakov VB (2009) Equilibrium iron isotope fractionation at core-mantle boundary conditions.
1278 *Science* 323:912–4. doi: 10.1126/science.1166329
- 1279 Polyakov VB, Clayton RN, Horita J, Mineev SD (2007) Equilibrium iron isotope fractionation factors
1280 of minerals- Reevaluation from the data of nuclear inelastic resonant X-ray scattering and
1281 Mössbauer spectroscopy.pdf. *Geochim Cosmochim Acta* 71:3833–3846.
- 1282 Polyakov VB, Kharlashina NN (1994) Effect of pressure on equilibrium isotopic fractionation.
1283 *Geochim Cosmochim Acta* 58:4739–4750.
- 1284 Polyakov VB, Mineev SD (2000) The use of Mössbauer spectroscopy in stable isotope geochemistry.
1285 *Geochim Cosmochim Acta* 64:849–865.
- 1286 Poustovetov AA, Roeder PL (2000) The distribution of Cr between basaltic melt and chromian spinel
1287 as an oxygen geobarometer. *Can Mineral* 39:309–317.
- 1288 Richards JP (2011) Magmatic to hydrothermal metal fluxes in convergent and collided margins. *Ore*
1289 *Geol Rev* 40:1–26. doi: 10.1016/j.oregeorev.2011.05.006
- 1290 Roskosz M, Sio CKI, Dauphas N, Bi W (2015) Spinel – olivine – pyroxene equilibrium iron isotopic
1291 fractionation and applications to natural peridotites. 169:184–199. doi:
1292 10.1016/j.gca.2015.07.035
- 1293 Rouxel O, Dobbek N, Ludden J, Fouquet Y (2003) Iron isotope fractionation during oceanic crust
1294 alteration. *Chem Geol* 202:155–182. doi: 10.1016/j.chemgeo.2003.08.011
- 1295 Rustad JR, Yin Q-Z (2009) Iron isotope fractionation in the Earth’s lower mantle. *Nat Geosci* 2:514–
1296 518. doi: 10.1038/ngeo546
- 1297 Sanchez-Valle C, Hin RC, Testemale D, et al (2017) Stability of oxidized iron species and the redox
1298 budget of slab-derived fluids. In: American Geophysical Union, Fall Meeting. p V11D–01
- 1299 Sanloup C, Drewitt JWE, Konôpková Z, et al (2013) Structural change in molten basalt at deep
1300 mantle conditions. *Nature* 503:104–107. doi: 10.1038/nature12668
- 1301 Saunier G, Pokrovski GS, Poitrasson F (2011) First experimental determination of iron isotope
1302 fractionation between hematite and aqueous solution at hydrothermal conditions. *Geochim*
1303 *Cosmochim Acta* 75:6629–6654. doi: 10.1016/j.gca.2011.08.028
- 1304 Scambelluri M, Pettke T, Cannaò E (2015) Fluid-related inclusions in Alpine high-pressure peridotite
1305 reveal trace element recycling during subduction-zone dehydration of serpentized mantle
1306 (Cima di Gagnone, Swiss Alps). *Earth Planet Sci Lett* 429:45–59. doi:
1307 10.1016/j.epsl.2015.07.060
- 1308 Scambelluri M, Pettke T, Rampone E, et al (2014) Petrology and trace element budgets of high-
1309 pressure peridotites indicate subduction dehydration of serpentized mantle (Cima di Gagnone,
1310 Central Alps, Switzerland). *J Petrol* 55:459–498. doi: 10.1093/petrology/egt068
- 1311 Schauble E (2004) Applying stable isotope fractionation theory to new systems. *Rev Mineral*
1312 *Geochemistry* 55:65. doi: 10.2138/gsrng.55.1.65
- 1313 Schauble EA, Rossman GR, Taylor HP (2001) Theoretical estimates of equilibrium Fe-isotope
1314 fractionations from vibrational spectroscopy. *Geochim Cosmochim Acta* 65:2487–2497.
- 1315 Schmidt MW, Poli S (1998) Experimentally based water budgets for dehydrating slabs and
1316 consequences for arc magma generation. *Earth Planet Sci Lett* 163:361–379. doi:

- 1317 10.1016/S0012-821X(98)00142-3
- 1318 Schoenberg R, Marks MA, Schuessler JA, et al (2009) Fe isotope systematics of coexisting amphibole
1319 and pyroxene in the alkaline igneous rock suite of the Ilímaussaq Complex, South Greenland.
1320 *Chem Geol* 258:65–77.
- 1321 Schoenberg R, von Blanckenburg F (2006) Modes of planetary-scale Fe isotope fractionation. *Earth*
1322 *Planet Sci Lett* 252:342–359. doi: 10.1016/j.epsl.2006.09.045
- 1323 Schuessler JA, Schoenberg R, Sigmarsson O (2009) Iron and lithium isotope systematics of the Hekla
1324 volcano, Iceland — Evidence for Fe isotope fractionation during magma differentiation. *Chem*
1325 *Geol* 258:78–91.
- 1326 Severmann S, Johnson CM, Beard BL, et al (2004) The effect of plume processes on the Fe isotope
1327 composition of hydrothermally derived Fe in the deep ocean as inferred from the Rainbow vent
1328 site, Mid-Atlantic Ridge, 36°14'N. *Earth Planet Sci Lett* 225:63–76. doi:
1329 10.1016/j.epsl.2004.06.001
- 1330 Shahar A, Elardo SM, Macris CA (2017) Equilibrium fractionation of non-traditional stable isotopes:
1331 an experimental perspective. *Rev Mineral Geochemistry* 82:65–83. doi: 10.2138/rmg.2017.82.3
- 1332 Shahar A, Schauble EA, Caracas R, et al (2016) Pressure-dependent isotopic composition of iron
1333 alloys. *Science (N.Y.)* 353:580–582. doi: 10.1126/science.aad9945
- 1334 Shahar A, Young ED, Manning CE (2008) Equilibrium high-temperature Fe isotope fractionation
1335 between fayalite and magnetite: An experimental calibration. *Earth Planet Sci Lett* 268:330–338.
1336 doi: 10.1016/j.epsl.2008.01.026
- 1337 Shanks WC, Bischoff JL, Rosenbauer RJ (1981) Seawater sulfate reduction and sulfur isotope
1338 fractionation in basaltic systems: Interaction of seawater with fayalite and magnetite at 200-
1339 350°C. *Geochim Cosmochim Acta* 45:1977–1995. doi: 10.1016/0016-7037(81)90054-5
- 1340 Simon AC, Pettke T, Candela PA, et al (2004) Magnetite solubility and iron transport in magmatic-
1341 hydrothermal environments. *Geochim Cosmochim Acta* 68:4905–4914. doi:
1342 10.1016/j.gca.2004.05.033
- 1343 Smythe DJ, Wood BJ, Kiseeva ES (2017) The S content of silicate melts at sulfide saturation: New
1344 experiments and a model incorporating the effects of sulfide composition. *Am Mineral* 102:795–
1345 803. doi: 10.2138/am-2017-5800CCBY
- 1346 Sossi PA, Foden JD, Halverson GP (2012) Redox-controlled iron isotope fractionation during
1347 magmatic differentiation: an example from the Red Hill intrusion, S. Tasmania. *Contrib to*
1348 *Mineral Petrol* 164:757–772. doi: 10.1007/s00410-012-0769-x
- 1349 Sossi PA, Halverson GP, Nebel O, Eggins SM (2015) Combined Separation of Cu, Fe and Zn from
1350 Rock Matrices and Improved Analytical Protocols for Stable Isotope Determination. *Geostand*
1351 *Geoanalytical Res* 39:129–149. doi: 10.1111/j.1751-908X.2014.00298.x
- 1352 Sossi PA, Nebel O, Foden J (2016) Iron isotope systematics in planetary reservoirs. *Earth Planet Sci*
1353 *Lett* 452:295–308. doi: 10.1016/j.epsl.2016.07.032
- 1354 Sossi PA, O'Neill HSC (2017) The effect of bonding environment on iron isotope fractionation
1355 between minerals at high temperature. *Geochim Cosmochim Acta* 196:121–143. doi:
1356 10.1016/j.gca.2016.09.017
- 1357 Su BX, Teng F-Z, Hu Y, et al (2015) Iron and magnesium isotope fractionation in oceanic lithosphere
1358 and sub-arc mantle: Perspectives from ophiolites. *Earth Planet Sci Lett* 430:523–532. doi:
1359 10.1016/j.epsl.2015.08.020
- 1360 Syverson DD, Borrok D, Seyfried WE (2013) Experimental determination of equilibrium Fe isotopic
1361 fractionation between pyrite and dissolved Fe under hydrothermal conditions. *Geochim*

- 1362 Cosmochim Acta 122:170–183.
- 1363 Syverson DD, Luhmann AJ, Tan C, et al (2017) Fe isotope fractionation between chalcopyrite and
1364 dissolved Fe during hydrothermal recrystallization: An experimental study at 350 °C and
1365 500 bars. *Geochim Cosmochim Acta* 200:87–109. doi: 10.1016/J.GCA.2016.12.002
- 1366 Teng F-Z, Dauphas N, Helz RT (2008) Iron isotope fractionation during magmatic differentiation in
1367 Kilauea Iki lava lake. *Science* 320:1620–2. doi: 10.1126/science.1157166
- 1368 Teng F-Z, Dauphas N, Huang S, Marty B (2013) Iron isotopic systematics of oceanic basalts.
1369 *Geochim Cosmochim Acta* 107:12–26.
- 1370 Testemale D, Brugger J, Liu W, et al (2009) In-situ X-ray absorption study of Iron(II) speciation in
1371 brines up to supercritical conditions. *Chem Geol* 264:295–310. doi:
1372 10.1016/j.chemgeo.2009.03.014
- 1373 Toplis MJ (2005) The thermodynamics of iron and magnesium partitioning between olivine and
1374 liquid: criteria for assessing and predicting equilibrium in natural and experimental systems.
1375 *Contrib to Mineral Petrol* 149:22–39. doi: 10.1007/s00410-004-0629-4
- 1376 Toplis MJ, Carroll MR (1995) An Experimental Study of the Influence of Oxygen Fugacity on Fe-Ti
1377 Oxide Stability, Phase Relations, and Mineral-Melt Equilibria in Ferro-Basaltic Systems.
1378 *Contrib to Mineral Petrol* 36:1137–1170.
- 1379 Toplis MJ, Carroll MR (1996) Differentiation of Ferro-Basaltic Magmas under Conditions Open and
1380 Closed to Oxygen : Implications for the Skaergaard Intrusion and Other Natural Systems.
1381 *Contrib to Mineral Petrol* 37:837–858.
- 1382 Trommsdorff V, López Sánchez-Vizcaíno V, Gómez-Pugnaire MT, Müntener O (1998) High pressure
1383 breakdown of antigorite to spinifex-textured olivine and orthopyroxene, SE Spain. *Contrib to*
1384 *Mineral Petrol* 132:139–148. doi: 10.1007/s004100050412
- 1385 Turner SP, Foden JD, Morrison RS (1992) Derivation of some A-type magmas by fractionation of
1386 basaltic magma: An example from the Padthaway Ridge, South Australia. *Lithos* 28:151–179.
- 1387 Turner SP, Williams HM, Piazzolo S, et al (2018) Sub-arc xenolith Fe-Li-Pb isotopes and textures tell
1388 tales of their journey through the mantle wedge and crust. *Geology* 46:947–950. doi:
1389 10.1130/G45359.1
- 1390 Urey HC (1947) The thermodynamic properties of isotopic substances. *J Chem Soc* 562–581.
- 1391 Urosevic M, Nebel O, Padron-Navarta JA, Rubatto D (2018) Assessment of O and Fe isotope
1392 heterogeneity in garnet from Kakanui (New Zealand) and Erongo (Namibia). *Eur J Mineral.* doi:
1393 10.1029/EO060i020p00457-02
- 1394 Vanpeteghem CB, Angel RJ, Ross NL, et al (2006) Al, Fe substitution in the MgSiO₃ perovskite
1395 structure: A single-crystal X-ray diffraction study. *Phys Earth Planet Inter* 155:96–103. doi:
1396 10.1016/J.PEPI.2005.10.003
- 1397 Wallace PJ, Edmonds M (2011) The Sulfur Budget in Magmas: Evidence from Melt Inclusions,
1398 Submarine Glasses, and Volcanic Gas Emissions. *Rev Mineral Geochemistry* 73:215–246. doi:
1399 10.2138/rmg.2011.73.8
- 1400 Wawryk CM, Foden JD (2015) Fe-isotope fractionation in magmatic-hydrothermal mineral deposits:
1401 A case study from the Renison Sn-W deposit, Tasmania. *Geochim Cosmochim Acta* 150:285–
1402 298. doi: 10.1016/j.gca.2014.09.044
- 1403 Wawryk CM, Foden JD (2017) Iron-isotope systematics from the Batu Hijau Cu-Au deposit,
1404 Sumbawa, Indonesia. *Chem Geol* 466:159–172. doi: 10.1016/J.CHEMGEO.2017.06.004
- 1405 Wechsler BA, Lindsley DH, Prewitt CT (1984) Crystal structure and cation distribution in

- 1406 titanomagnetites ($\text{Fe}_{3-x}\text{Ti}_x\text{O}_4$). *Am Mineral* 69:754–770.
- 1407 Wechsler BA, Prewitt CT (1984) Crystal structure of ilmenite (FeTiO_3) at high temperature and at
1408 high pressure. *Am Mineral* 69:176–185.
- 1409 Wentzcovitch RM, Justo JF, Wu Z, et al (2009) Anomalous compressibility of ferropericlasite
1410 throughout the iron spin cross-over. *Proc Natl Acad Sci U S A* 106:8447–52. doi:
1411 10.1073/pnas.0812150106
- 1412 Weyer S, Anbar A, Brey G, et al (2005) Iron isotope fractionation during planetary differentiation.
1413 *Earth Planet Sci Lett* 240:251–264. doi: 10.1016/j.epsl.2005.09.023
- 1414 Weyer S, Ionov DA (2007) Partial melting and melt percolation in the mantle: The message from Fe
1415 isotopes. *Earth Planet Sci Lett* 259:119–133. doi: 10.1016/j.epsl.2007.04.033
- 1416 Wilke M (2005) Fe in magma – An overview. *Ann Geophys* 48:609–617.
- 1417 Wilke M, Farges F, Partzsch GM, et al (2007) Speciation of Fe in silicate glasses and melts by in-situ
1418 XANES spectroscopy. *Am Mineral* 92:44–56. doi: 10.2138/am.2007.1976
- 1419 Williams HM, Bizimis M (2014) Iron isotope tracing of mantle heterogeneity within the source
1420 regions of oceanic basalts. *Earth Planet Sci Lett* 404:396–407. doi: 10.1016/j.epsl.2014.07.033
- 1421 Williams HM, McCammon CA, Peslier AH, et al (2004) Iron isotope fractionation and the oxygen
1422 fugacity of the mantle. *Science* 304:1656–9. doi: 10.1126/science.1095679
- 1423 Williams HM, Nielsen SG, Renac C, et al (2009) Fractionation of oxygen and iron isotopes by partial
1424 melting processes: Implications for the interpretation of stable isotope signatures in mafic rocks.
1425 *Earth Planet Sci Lett* 283:156–166. doi: 10.1016/j.epsl.2009.04.011
- 1426 Williams HM, Peslier AH, McCammon C, et al (2005) Systematic iron isotope variations in mantle
1427 rocks and minerals: The effects of partial melting and oxygen fugacity. *Earth Planet Sci Lett*
1428 235:435–452.
- 1429 Williams HM, Prytulak J, Woodhead JD, et al (2018) Interplay of crystal fractionation, sulfide
1430 saturation and oxygen fugacity on the iron isotope composition of arc lavas: An example from
1431 the Marianas. *Geochim Cosmochim Acta* 226:224–243. doi: 10.1016/j.gca.2018.02.008
- 1432 Williams HM, Wood BJ, Wade J, et al (2012) Isotopic evidence for internal oxidation of the Earth's
1433 mantle during accretion. *Earth Planet Sci Lett* 321-322:54–63. doi: 10.1016/j.epsl.2011.12.030
- 1434 Woodhead J, Eggins S, Gamble J (1993) High field strength and transition element systematics in
1435 island arc and back-arc basin basalts: evidence for multi-phase melt extraction and a depleted
1436 mantle wedge. *Earth Planet Sci Lett* 114:491–504.
- 1437 Woodland AB, Kornprobst J, Wood BJ (1992) Oxygen Thermobarometry of Orogenic Lherzolite
1438 Massifs. *J Petrol* 33:203–230. doi: 10.1093/petrology/33.1.203
- 1439 Wu CC, Mason TO (1981) Thermopower Measurement of Cation Distribution in Magnetite. *J Am*
1440 *Ceram Soc* 64:520–522. doi: 10.1111/j.1151-2916.1981.tb10317.x
- 1441 Wu H, He Y, Bao L, et al (2017) Mineral composition control on inter-mineral iron isotopic
1442 fractionation in granitoids. *Geochim Cosmochim Acta* 198:208–217. doi:
1443 10.1016/j.gca.2016.11.008
- 1444 Xia Y, Li S, Huang F (2017) Iron and Zinc isotope fractionation during magmatism in the continental
1445 crust: Evidence from bimodal volcanic rocks from Hailar basin, NE China. *Geochim*
1446 *Cosmochim Acta* 213:35–46. doi: 10.1016/j.gca.2017.06.018
- 1447 Yang H, Lin J-F, Hu MY, et al (2019) Iron isotopic fractionation in mineral phases from Earth's
1448 lower mantle: Did terrestrial magma ocean crystallization fractionate iron isotopes? *Earth Planet*

- 1449 Sci Lett 506:113–122. doi: 10.1016/J.EPSL.2018.10.034
- 1450 Young ED, Manning CE, Schauble EA, et al (2015) High-temperature equilibrium isotope
1451 fractionation of non-traditional stable isotopes: Experiments, theory, and applications. Chem
1452 Geol 395:176–195. doi: 10.1016/j.chemgeo.2014.12.013
- 1453 Young ED, Tonui E, Manning CE, et al (2009) Spinel–olivine magnesium isotope thermometry in the
1454 mantle and implications for the Mg isotopic composition of Earth. Earth Planet Sci Lett
1455 288:524–533.
- 1456 Zhang HL, Hirschmann MM, Cottrell E, Withers AC (2017) Effect of pressure on $\text{Fe}^{3+}/\Sigma\text{Fe}$ ratio in a
1457 mafic magma and consequences for magma ocean redox gradients. Geochim Cosmochim Acta
1458 204:83–103. doi: 10.1016/J.GCA.2017.01.023
- 1459 Zhang L, Sun W, Zhang Z, et al (2019) Iron isotopic composition of supra-subduction zone ophiolitic
1460 peridotites from northern Tibet. Geochim Cosmochim Acta 258:274–289. doi:
1461 10.1016/J.GCA.2019.04.031
- 1462 Zhao X, Zhang H, Zhu X, et al (2010) Iron isotope variations in spinel peridotite xenoliths from North
1463 China Craton: Implications for mantle metasomatism. Contrib to Mineral Petrol 160:1–14. doi:
1464 10.1007/s00410-009-0461-y
- 1465 Zhao X, Zhang H, Zhu X, et al (2012) Iron isotope evidence for multistage melt–peridotite
1466 interactions in the lithospheric mantle of eastern China. Chem Geol 292-293:127–139. doi:
1467 10.1016/j.chemgeo.2011.11.016
- 1468 Zhao X, Zhang Z, Huang S, et al (2017) Coupled extremely light Ca and Fe isotopes in peridotites.
1469 Geochim Cosmochim Acta 208:368–380. doi: 10.1016/j.gca.2017.03.024
- 1470 Zhu XK, Guo Y, O’Nions RK, et al (2001) Isotopic homogeneity of iron in the early solar nebula.
1471 Nature 412:311–3. doi: 10.1038/35085525
- 1472
- 1473

1474 **Figure Captions**

1475 **Fig. 1.** After Sossi and O'Neill (2017). Dependence of the calculated force constants on the co-ordination number and oxidation
 1476 state of iron. Lines of constant $\text{Fe}^{3+}/\Sigma\text{Fe}$ are drawn on in black. Effects of two common solid solutions on the force constant
 1477 (magnetite–ulvöspinel and hematite–ilmenite) are shown in grey. Minerals are shown in white squares; Her = Hercynite, Chr
 1478 = Chromite, Usp = Ulvöspinel, Mag = Magnetite, Hem = Hematite, Ilm = Ilmenite, Fay = Fayalite, Alm = Almandine.

1479 **Fig. 2.** Iron-oxygen force constant in spinel group minerals (after Roskosz et al. 2015). The regression and associated
 1480 uncertainty refers to Al-bearing spinels only, and the rhyolite and basalt trend are from the data of Dauphas et al. (2014). P&M
 1481 = Polyakov and Mineev 2000; P = Polyakov et al., 2007; M = Mineev et al. 2007; D = Dauphas et al. 2012.

1482 **Fig. 3.** After Dauphas et al. (2014). Mean force constants of Fe-O bonds in silicate glasses for basalt (circle), andesite (square),
 1483 dacite (triangle) and rhyolite (diamond) compositions as a function of their $\text{Fe}^{3+}/\Sigma\text{Fe}$ content measured by XANES. The linear
 1484 trends defined by the data permit extrapolation of Fe-O force constants to $\text{Fe}^{3+}/\Sigma\text{Fe} = 1$. Uncertainties on the error envelopes
 1485 are 95% confidence intervals.

1486 **Fig. 4.** After Liu et al. (2017). Force constants (N/m) of iron bonds in Fe^{3+} -free basaltic glass (black squares) with their
 1487 associated 95% confidence intervals as a function of pressure (GPa) at room temperature (300 K). Black lines are linear fits to
 1488 the data. Also shown are iron force constants in bridgmanite (Rustad and Yin, 2009, dashed line and Shahar et al., 2016, purple
 1489 square).

1490 **Fig. 5.** After Fujii et al. 2014. Temperature dependence of the $10^3 \ln \beta^{56/54}\text{Fe}$ for aqueous a) Fe^{2+} and b) Fe^{3+} species. The vertical
 1491 scale factor of b) is $1.5\times$ that of a).

1492 **Fig. 6.** Melting models from Sossi & O'Neill (2017) (see eqs. 21–24). *a*) Variation of the fractionation factor between liquid
 1493 and solid as a function of source lithology and degree of melting. Peridotites in the spinel (sp) and garnet (gt) fields show
 1494 similar fractionation, whereas partial melts of eclogites (ecl) have a more pronounced enrichment in heavy isotopes. *b*)
 1495 Variation of the fractionation factor between solid and liquid as a function of $\text{Fe}^{3+}/\Sigma\text{Fe}_{\text{Melt}}$ for three different source
 1496 compositions; 'Ox' = oxidised ($\text{Fe}^{3+}/\Sigma\text{Fe}_{\text{Source}} = 0.051$), 'Int' = intermediate ($\text{Fe}^{3+}/\Sigma\text{Fe}_{\text{Source}} = 0.036$), 'Red' = reduced
 1497 ($\text{Fe}^{3+}/\Sigma\text{Fe}_{\text{Source}} = 0.021$). Dashed lines are fraction of melting (F) contours, listed to their right. Melting of more oxidised
 1498 sources is associated with greater isotopic fractionation.

1499 **Fig. 7.** After Sossi and O'Neill (2017). Iron isotope composition of mafic rocks (black triangle, MORB; white square, Hawai'i;
 1500 grey circle, Tahiti) from the ocean basins (Teng et al., 2013), corrected to their primary magma compositions, plotted against
 1501 Gd/Yb_N . Black lines show the iron isotope compositions of melts modelled by batch melting (Eq. (21)), at melt fractions given
 1502 in grey, in both the garnet (gt) and spinel (sp) fields from a primitive mantle source (grey star), and of eclogite partial melts
 1503 (ec), from an N-MORB source ($\delta^{57}\text{Fe} = +0.1\text{‰}$).

1504 **Fig. 8.** After Foden et al. (2018). $\delta^{57}\text{Fe}_{(\text{IRMM-14})}$ vs. Slab Thermal Parameter (φ)/100km for population means for each arc or
 1505 arc segment. The error bars are 2SE and the 95% uncertainty envelope of the linear regression is indicated as the black curves.
 1506 Value for MORB is from Teng et al. (2013).

1507 **Fig. 9.** After Heimann et al. 2008. An early compilation of iron isotope analyses in igneous rocks.

1508 **Fig. 10.** $\delta^{57}\text{Fe}$ of whole rocks against their Mg#, characterising the change in iron isotope composition with differentiation. *a*)
 1509 Analyses of co-genetic whole-rock samples from tholeiitic suites: green squares = Kilauea Iki (Teng et al. 2008), blue
 1510 diamonds = Hekla (Schuessler et al. 2009), orange circles = Red Hill (Sossi et al. 2012) display disparate behaviour depending
 1511 on whether the system evolved open (Hekla) or closed (Red Hill, Kilauea Iki) to oxygen exchange (see Systems open and
 1512 closed to oxygen exchange). *b*) Simplified versions of Figs 4 and 7 from Toplis and Carroll (1996), highlighting the contrasting

1513 change in fO_2 relative to the FMQ buffer and Fe_2O_3 (wt. %) for conditions open and closed to oxygen exchange, respectively.
1514 These trends directly mirror those seen in a.

1515 **Fig. 11.** After Du et al. 2017. Compilation of Fe isotope mineral compositions in igneous rocks.

1516 Fig. 12: After Debret et al. (2016). Increase in $\delta^{56}Fe$ and decrease of $Fe^{3+}/\Sigma Fe$ ratio in serpentinites during subduction. Bulk
1517 sample iron isotope composition versus $Fe^{3+}/\Sigma Fe$ in subducted Alpine lizardite (Liz-) and antigorite (Atg/Liz- and Atg-)
1518 bearing serpentinites are compared to the one of abyssal serpentinites.

1519

For Review Only

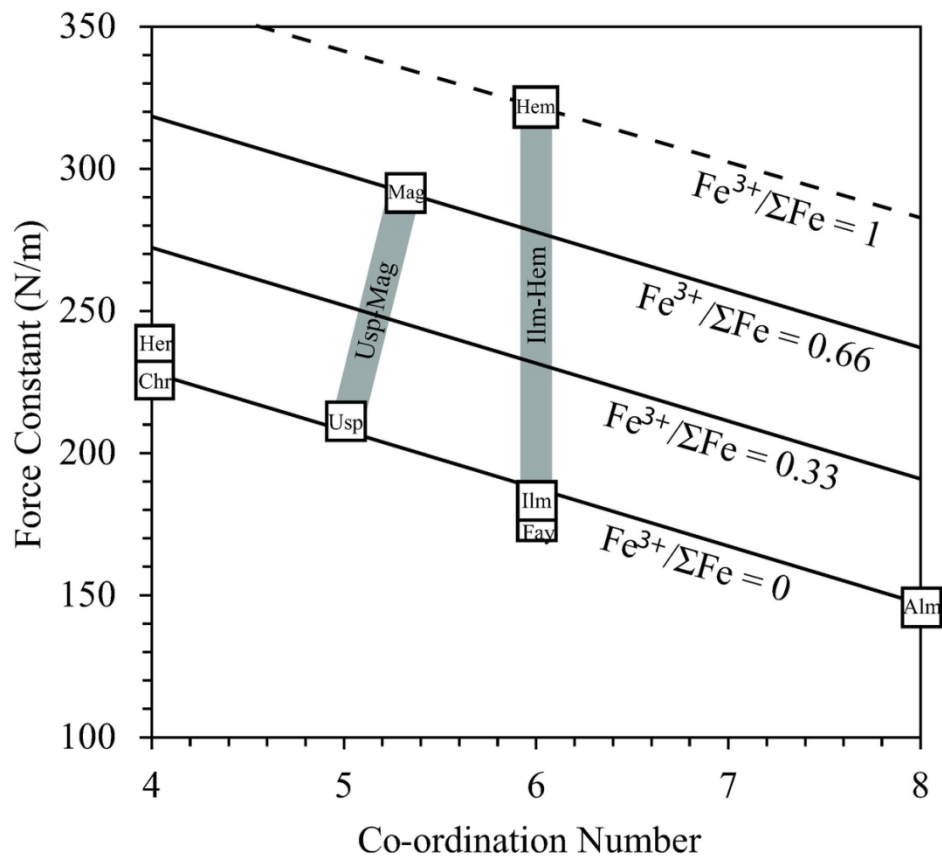


Fig. 1. After Sossi and O'Neill (2017). Dependence of the calculated force constants on the co-ordination number and oxidation state of iron. Lines of constant $Fe^{3+}/\Sigma Fe$ are drawn on in black. Effects of two common solid solutions on the force constant (magnetite-ulvöspinel and hematite-ilmenite) are shown in grey. Minerals are shown in white squares; Her = Hercynite, Chr = Chromite, Usp = Ulvöspinel, Mag = Magnetite, Hem = Hematite, Ilm = Ilmenite, Fay = Fayalite, Alm = Almandine.

112x102mm (300 x 300 DPI)

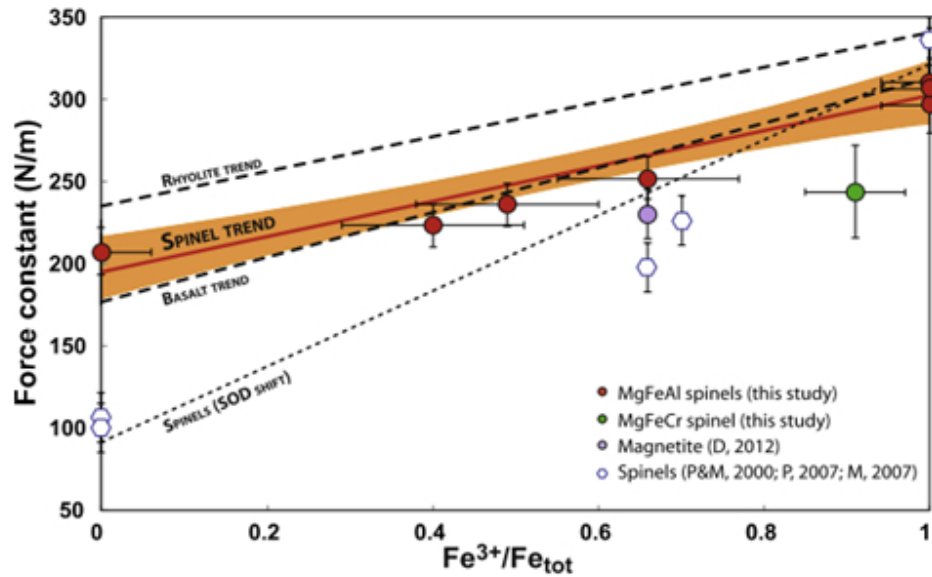


Fig. 2. Iron-oxygen force constant in spinel group minerals (after Roskosz et al. 2015). The regression and associated uncertainty refers to Al-bearing spinels only, and the rhyolite and basalt trend are from the data of Dauphas et al. (2014). P&M = Polyakov and Mineev 2000; P = Polyakov et al., 2007; M = Mineev et al. 2007; D = Dauphas et al. 2012.

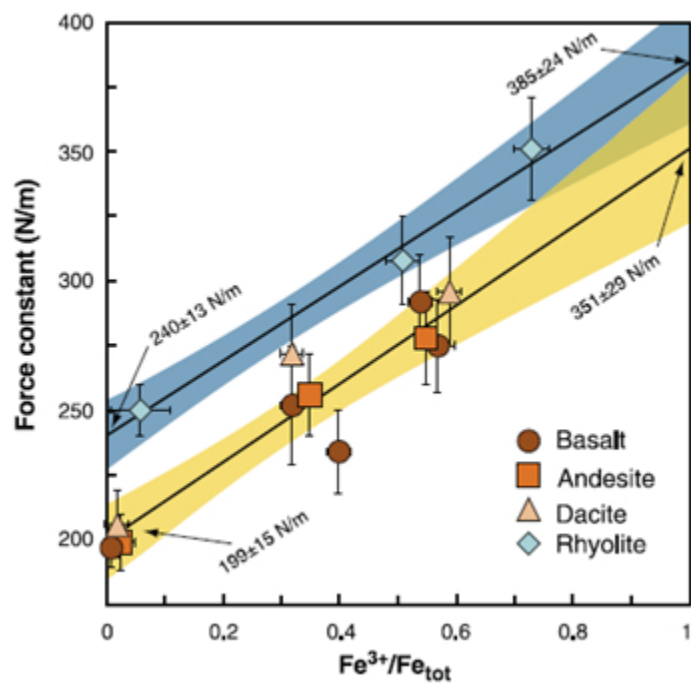


Fig. 3. After Dauphas et al. (2014). Mean force constants of Fe-O bonds in silicate glasses for basalt (circle), andesite (square), dacite (triangle) and rhyolite (diamond) compositions as a function of their $Fe^{3+}/\Sigma Fe$ content measured by XANES. The linear trends defined by the data permit extrapolation of Fe-O force constants to $Fe^{3+}/\Sigma Fe = 1$. Uncertainties on the error envelopes are 95% confidence intervals.

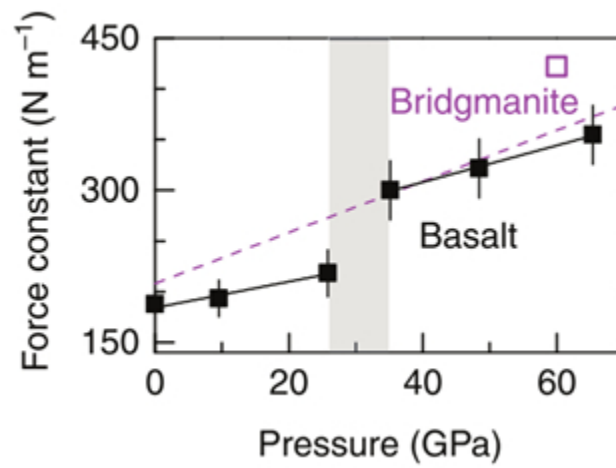


Fig. 4. After Liu et al. (2017). Force constants (N/m) of iron bonds in Fe³⁺-free basaltic glass (black squares) with their associated 95% confidence intervals as a function of pressure (GPa) at room temperature (300 K). Black lines are linear fits to the data. Also shown are iron force constants in bridgmanite (Rustad and Yin, 2009, dashed line and Shahar et al., 2016, purple square).

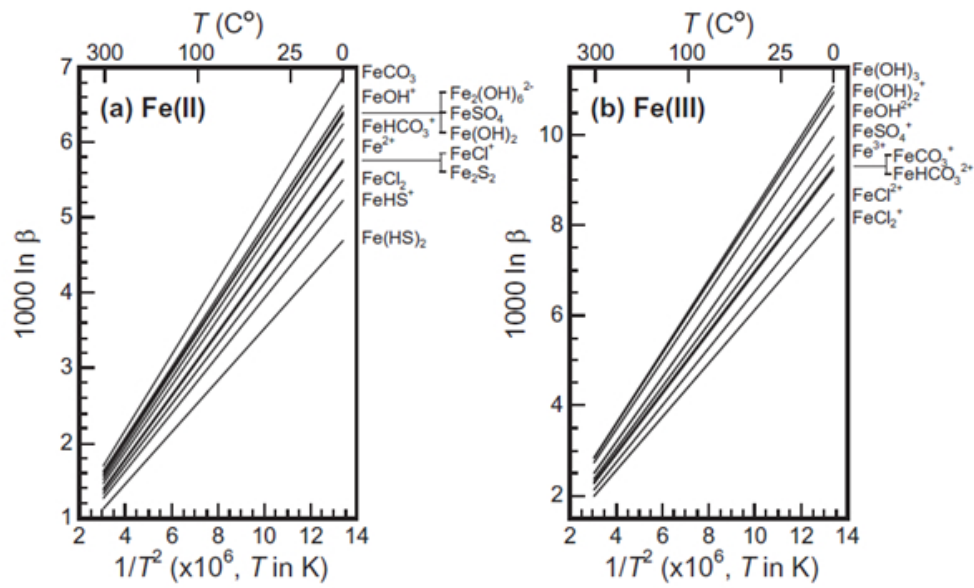


Fig. 5. After Fujii et al. 2014. Temperature dependence of the $10^3 \ln \beta^{56/54}\text{Fe}$ for aqueous a) Fe^{2+} and b) Fe^{3+} species. The vertical scale factor of b) is $1.5\times$ that of a).

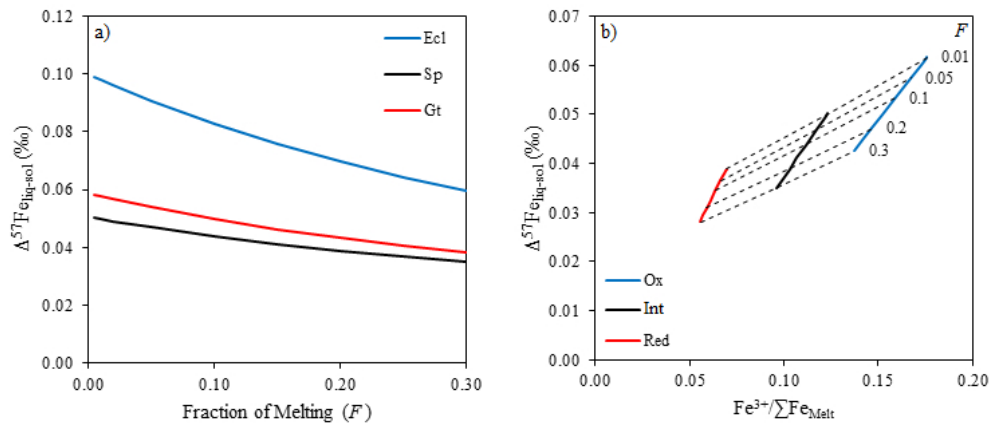


Fig. 6. Melting models from Sossi & O'Neill (2017) (see eqs. 21-24). a) Variation of the fractionation factor between liquid and solid as a function of source lithology and degree of melting. Peridotites in the spinel (sp) and garnet (gt) fields show similar fractionation, whereas partial melts of eclogites (ecl) have a more pronounced enrichment in heavy isotopes. b) Variation of the fractionation factor between solid and liquid as a function of $\text{Fe}^{3+}/\Sigma\text{Fe}_{\text{Melt}}$ for three difference source compositions; 'Ox' = oxidised ($\text{Fe}^{3+}/\Sigma\text{Fe}_{\text{Source}} = 0.051$), 'Int' = intermediate ($\text{Fe}^{3+}/\Sigma\text{Fe}_{\text{Source}} = 0.036$), 'Red' = reduced ($\text{Fe}^{3+}/\Sigma\text{Fe}_{\text{Source}} = 0.021$). Dashed lines are fraction of melting (F) contours, listed to their right. Melting of more oxidised sources is associated with greater isotopic fractionation.

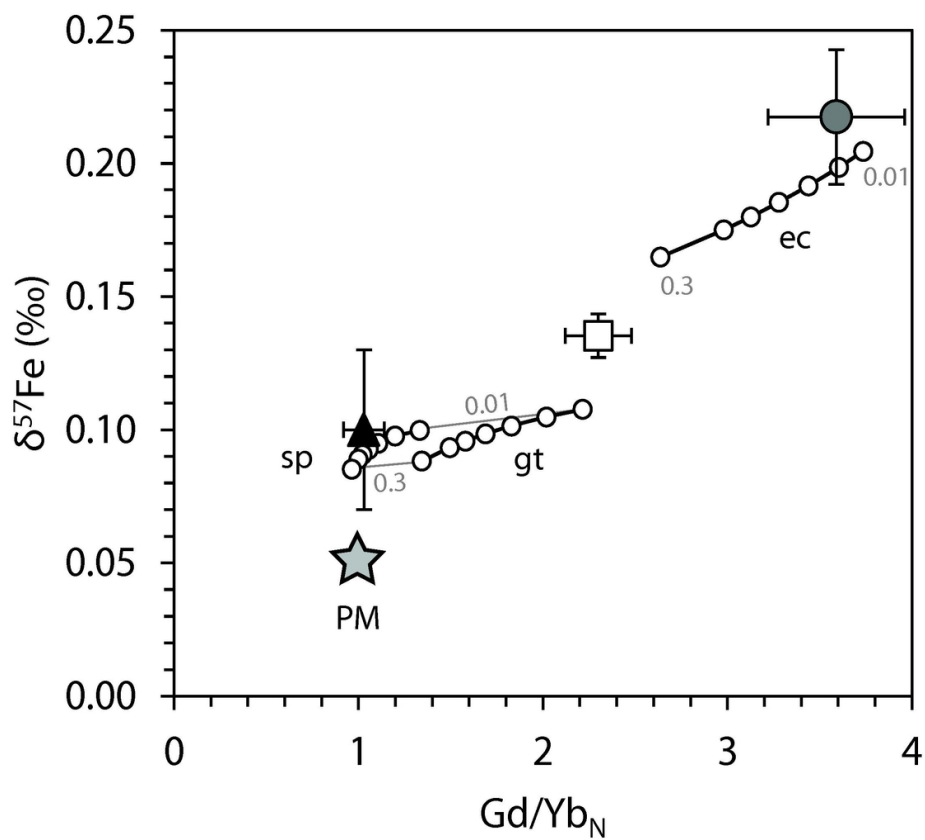


Fig. 7. After Sossi and O'Neill (2017). Iron isotope composition of mafic rocks (black triangle, MORB; white square, Hawai'i; grey circle, Tahiti) from the ocean basins (Teng et al., 2013), corrected to their primary magma compositions, plotted against Gd/Yb_N . Black lines show the iron isotope compositions of melts modelled by batch melting (Eq. (21)), at melt fractions given in grey, in both the garnet (gt) and spinel (sp) fields from a primitive mantle source (grey star), and of eclogite partial melts (ec), from an N-MORB source ($\delta^{57}\text{Fe} = +0.1\text{‰}$).

102x91mm (300 x 300 DPI)

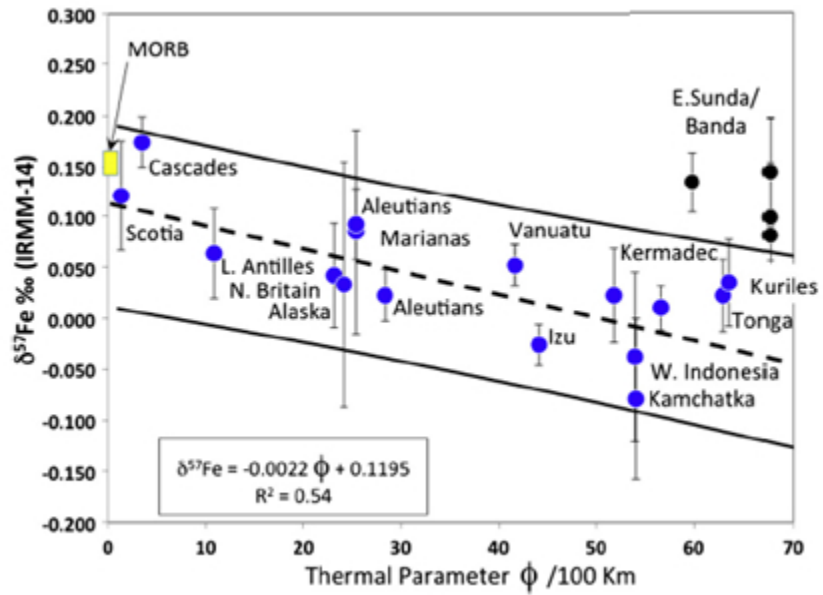


Fig. 8. After Foden et al. (2018). $\delta^{57}\text{Fe}(\text{IRMM-14})$ vs. Slab Thermal Parameter (ϕ)/100km for population means for each arc or arc segment. The error bars are 2SE and the 95% uncertainty envelope of the linear regression is indicated as the black curves. Value for MORB is from Teng et al. (2013).

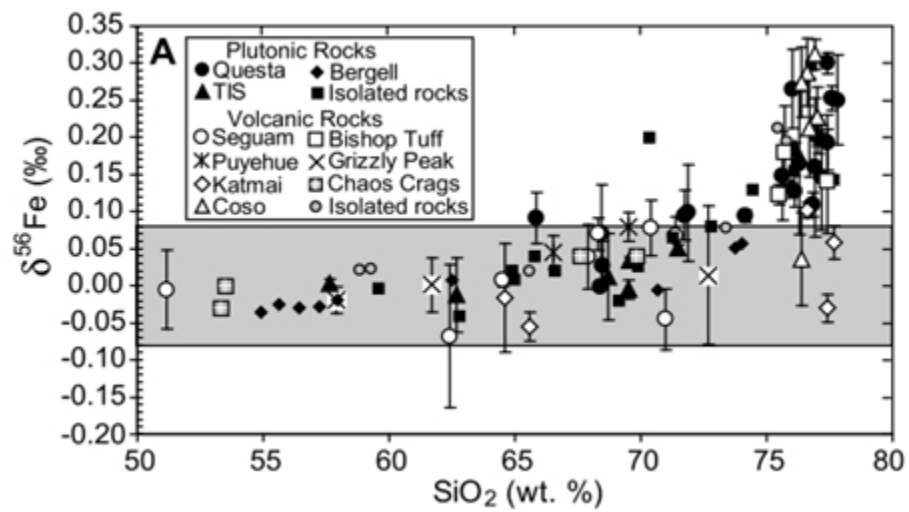


Fig. 9. After Heimann et al. 2008. An early compilation of iron isotope analyses in igneous rocks.

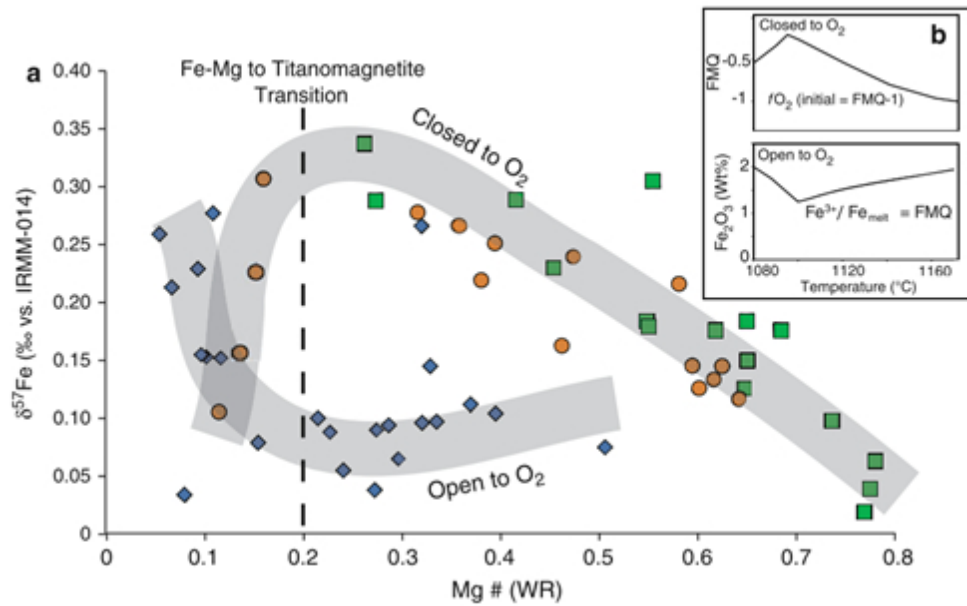


Fig. 10. $\delta^{57}\text{Fe}$ of whole rocks against their Mg#, characterising the change in iron isotope composition with differentiation. a) Analyses of co-genetic whole-rock samples from tholeiitic suites: green squares = Kilauea Iki (Teng et al. 2008), blue diamonds = Hekla (Schuessler et al. 2009), orange circles = Red Hill (Sossi et al. 2012) display disparate behaviour depending on whether the system evolved open (Hekla) or closed (Red Hill, Kilauea Iki) to oxygen exchange (see Systems open and closed to oxygen exchange). b) Simplified versions of Figs 4 and 7 from Toplis and Carroll (1996), highlighting the contrasting change in $f\text{O}_2$ relative to the FMQ buffer and Fe_2O_3 (wt. %) for conditions open and closed to oxygen exchange, respectively. These trends directly mirror those seen in a.

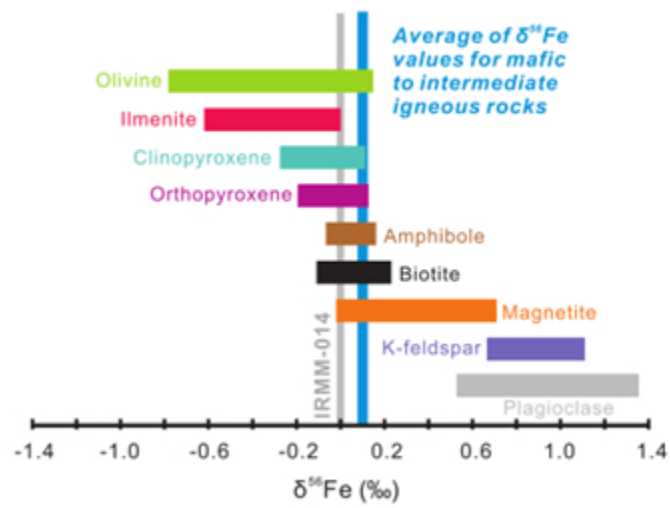


Fig. 11. After Du et al. 2017. Compilation of Fe isotope mineral compositions in igneous rocks.

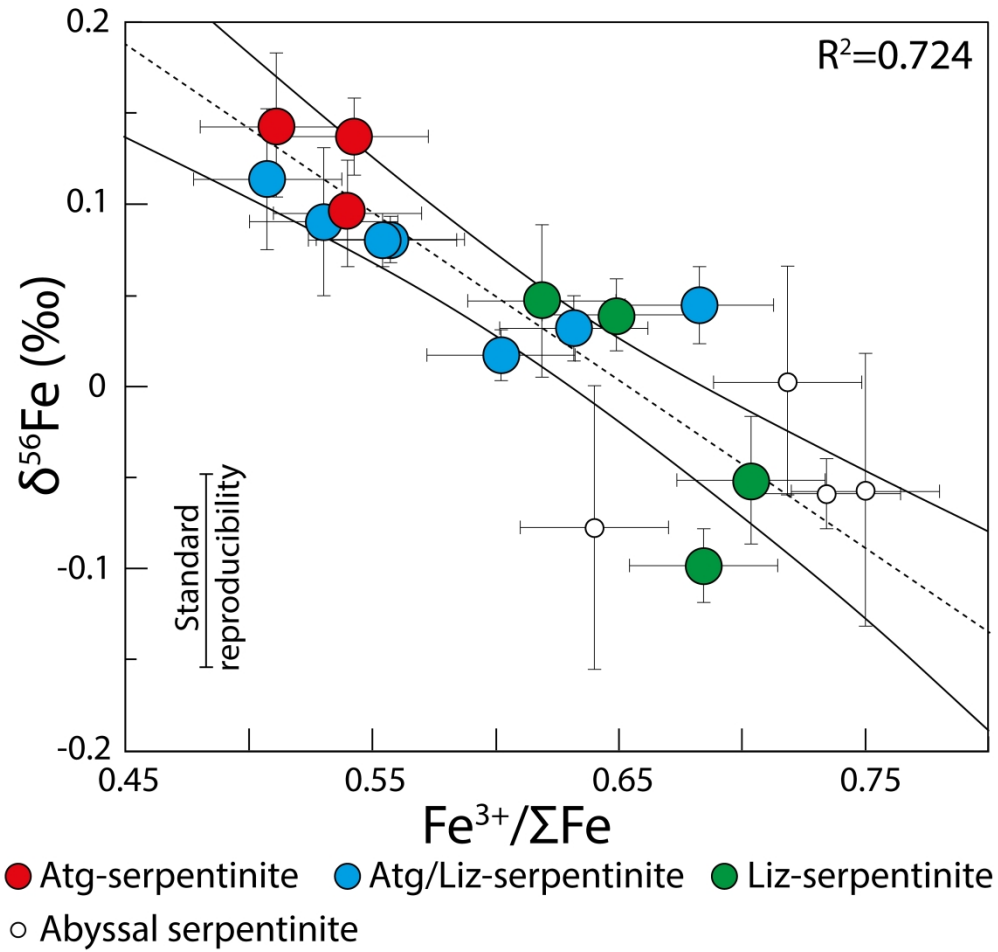


Fig. 12: After Debret et al. (2016). Increase in $\delta^{56}\text{Fe}$ and decrease of $\text{Fe}^{3+}/\Sigma\text{Fe}$ ratio in serpentinites during subduction. Bulk sample iron isotope composition versus $\text{Fe}^{3+}/\Sigma\text{Fe}$ in subducted Alpine lizardite (Liz-) and antigorite (Atg/Liz- and Atg-) bearing serpentinites are compared to the one of abyssal serpentinites.

416x395mm (300 x 300 DPI)